Thermal infrared dust optical depth and coarse-mode effective diameter retrieved from collocated MODIS and CALIOP observations

5   Jianyu Zheng[1,2], Zhibo Zhang[1,2,*], Hongbin Yu[3], Anne Garnier[4,5], Qianqian Song[1,2], Chenxi Wang[2,3], Claudia Di Biagio[6], Jasper F. Kok[7], Yevgeny Derimian[8], Claire Ryder[9]

[1]Department of Physics, University of Maryland Baltimore County, Baltimore, MD 21250, USA
[2]Goddard Earth Sciences Technology and Research II, University of Maryland Baltimore County, Baltimore, MD
10 21250, USA
[3]NASA Goddard Space Flight Center, Greenbelt, MD 20771, USA
[4]Science Systems and Applications, Inc., Hampton, VA, USA
[5]NASA Langley Research Center, Hampton, VA, USA
[6]Université Paris Cité and Univ Paris Est Creteil, CNRS, LISA, F-75013 Paris, France
15 [7]Department of Atmospheric and Oceanic Sciences, University of California, Los Angeles, CA 90095, USA
[8] French National Centre for Scientific Research | CNRS · Laboratoire d'optique atmosphérique (LOA)
[9] Department of Meteorology, University of Reading, Reading, UK.

Correspondence to: Zhibo Zhang (zzbatmos@umbc.edu)

Abstract.

20   In this study, we developed a novel algorithm based on the collocated Moderate Resolution Imaging Spectroradiometer (MODIS) thermal infrared (TIR) observations and dust vertical profiles from the Cloud-Aerosol Lidar with Orthogonal Polarization (CALIOP) to simultaneously retrieve dust aerosol optical depth at 10 μm ($DAOD_{10μm}$) and the coarse-mode dust effective diameter (D_{eff}) over global oceans. The accuracy of the D_{eff} retrieval is assessed by comparing the PSD corresponding to retrieved D_{eff} with the in-situ measured dust particle size
25 distributions (PSDs) from the AER-D, SAMUM-2 and SALTRACE field campaigns through case studies. The new $DAOD_{10μm}$ retrievals were evaluated first through comparisons with the collocated $DAOD_{10.6μm}$ retrieved from the combined Imaging Infrared Radiometer (IIR) and CALIOP observations from our previous study (Zheng et al. 2022). The pixel-to-pixel comparison of the two retrievals indicates a good agreement (R~0.7) and a significant reduction of (~50%) retrieval uncertainties largely thanks to the better constraint on dust size. In a climatological comparison, the
30 seasonal and regional (5°×2°) mean $DAOD_{10um}$ retrievals based on our combined MODIS and CALIOP method are in good agreement with the two independent Infrared Atmospheric Sounding Interferometer (IASI) products over three dust transport regions (i.e., North Atlantic (NA; R = 0.9), Indian Ocean (IO; R = 0.8) and North Pacific (NP; R = 0.7)).

    Using the new retrievals from 2013 to 2017, we performed a climatological analysis of coarse mode dust D_{eff} over
35 global oceans. We found that dust D_{eff} over IO and NP are up to 20% smaller than that over NA. Over NA in summer, we found a ~50% reduction of the number of retrievals with $D_{eff} > 5$ μm from 15°W to 35°W and a stable trend of D_{eff} average at 4.4 μm from 35°W throughout the Caribbean Sea (90°W). Over NP in spring, only ~5% of retrieved pixels with $D_{eff} > 5$ μm are found from 150°E to 180°, while the mean D_{eff} remains stable at 4.0 μm throughout eastern NP. To our best knowledge, this study is the first to retrieve both DAOD and coarse-mode dust particle size over global

40   oceans for multiple years. This retrieval dataset provides insightful information for evaluating dust long-wave
      radiative effects and coarse mode dust particle size in models.

1 Introduction

      Mineral dust (referred to as "dust") lifted by strong surface winds in arid and semi-arid regions (Ginoux et al., 2012)
      is the most abundant type of atmospheric aerosol in terms of dry mass (Kinne et al., 2006; Goudie, 1983). Once aloft,

45   dust particles can be carried by winds for long-range transport on intercontinental to hemispherical scales, exerting
      far-reaching impacts on the climate system (Shao et al., 2011; Choobari et al., 2014; Yu et al., 2013; Tegen and Fung,
      1994; Uno et al., 2009). For example, dust significantly influences the earth system's radiative budget by interacting
      with both shortwave (SW) solar and longwave (LW) terrestrial radiations, known as the direct radiative effects (DRE).
      Previous studies have found that on a global mean basis, the dust DRE at the top of the atmosphere (TOA) is generally

50   negative in SW (i.e., a cooling effect) but positive (i.e., a warming effect) in LW, although dust SW DRE can be
      positive over bright surfaces (Kok et al. 2017, Li et al. 2021, Di Biagio et al., 2021, Song et al. 2018, 2022). Despite
      this qualitative understanding, the quantification of dust net DRE (i.e., SW DRE + LW DRE) remains highly uncertain,
      in part due to the great spatiotemporal heterogeneity of dust properties such as dust loading, optically represented by
      dust aerosol optical depth (DAOD) (Huneeus et al., 2011), particle size distribution (PSD) (Kok et al. 2017, Adebiyi

55   and Kok, 2020a), particle shape, and refractive indices (RI) (Li et al., 2021). The dust-radiation interactions perturb
      the surface energy balance and atmospheric heating rate and hence the thermodynamic structure of the atmosphere
      (Helmert et al., 2007), which in turn affects boundary layer dynamics and cloud formation processes (Amiri-Farahani
      et al., 2017; Grogan et al., 2016; Zhang et al., 2007).

60   Satellite remote sensing is uniquely capable of measuring the spatiotemporal variation of dust properties on regional
      to global scales and over years and decades. Many methods have been developed to retrieve the column-integrated
      AOD in the visible spectrum (AOD_{VIS}) (e.g., 550 nm) from passive satellite observations in the visible (VIS) and near-
      infrared (NIR) spectrum, such as the Moderate Resolution Imaging Spectroradiometer (MODIS) (Levy et al., 2013,
      Hsu et al., 2013) and the Multi-angle Imaging Spectroradiometer (MISR) (Kahn et al., 2010). It should be noted that

65   these retrievals obtain the total AOD contributed by not only dust but also other types of aerosols. As a result, the
      fraction of dust AOD (DAOD) in VIS ($DAOD_{VIS}$) needs to be further separated from the total AOD_{VIS} for dust-focused
      studies. Some methods rely on model simulations of $DAOD_{VIS}/AOD_{VIS}$ (Gkikas et al., 2021) or non-dust AOD_{VIS}
      (Ridley et al., 2016). Others are based on the contrasting properties of dust in comparison with other aerosols, such as
      its larger size manifested as a smaller Angstrom Exponent and a smaller fine-mode fraction (Kaufman et al., 2005, Yu

70   et al., 2009, 2021) and significant spectral gradient in the absorption from deep blue to the VIS (Ginoux et al., 2010,
      Pu and Ginoux, 2018). In addition, the active spaceborne Lidars with VIS-NIR channels, such as the Cloud-Aerosol
      Lidar with Orthogonal Polarization (CALIOP) onboard the Cloud-Aerosol Lidar and Infrared Pathfinder Satellite
      Observations (CALIPSO) mission and the Cloud-Aerosol Transport System (CATS), can be used to estimate the
      vertical distribution of $DAOD_{VIS}$ based on the observed particulate depolarization ratios (Yu et al., 2015b; Proestakis

75   et al., 2018). By utilizing these retrieval methods, several studies further developed decade-long satellite data records

of DAOD$_{VIS}$ (Gkikas et al., 2022; Song et al., 2021), which are frequently used for dust studies such as estimations of dust DRE, interannual variability and trends of dust, and global dust cycles (Song et al., 2022; Logothetis et al., 2021; Kok et al., 2021b).

80   The VIS-NIR dust observations are useful, but they do not provide direct measurements of DAOD at LW and have weak sensitivity to coarse particles (Ryder et al., 2019). Extending observed DAOD from the VIS-NIR to TIR spectra depends strongly on dust PSD and RI assumptions (Song et al., 2018). Therefore, TIR observations are an indispensable complement with several unique advantages. Dust dominated by coarse mode particles is arguably the only predominant particle that can cause strong radiative signatures in the TIR spectrum (Desouza-Machado et al.,
85   2006). Therefore, using TIR observation has an inherent advantage of directly retrieving DAOD, in contrast to the VIS-NIR observations in which empirical methods need to be developed to separate dust from other types of aerosols. Zheng et al. (2022) showed that direct TIR observations could significantly reduce uncertainties in DAOD$_{TIR}$ and LW DRE associated with dust PSD and RI assumptions. Moreover, previous studies revealed that super-coarse dust particles ($D_p > 20$ μm) are ubiquitously detected from numerous in-situ measurements in both source regions and
90   transport regions (Weinzierl et al., 2017; Denjean et al., 2016; Ryder et al., 2013b; Ryder et al., 2018), which however is excluded or underestimated in most dust transport models (Checa-Garcia et al., 2021; Wu et al., 2020; Zhao et al., 2022). How many and how frequently can super-coarse dust particles be carried in long-range transport? The lack of observational data with finer spatiotemporal coverage prevents us from further revealing their transport patterns. TIR satellite observations with great sensitivity to super coarse particles can potentially fill this knowledge gap.

95

Notwithstanding the advantages, retrieving dust properties in TIR, particularly the dust particle size, usually represented by effective radius or diameter, is challenging. In the past, TIR dust retrieval algorithms were primarily based on observations from space-borne hyperspectral atmospheric sounders, such as the Advanced Infrared Radiation Sounder (AIRS) and the Infrared Atmospheric Sounding Interferometer (IASI). The important advantages of
100   hyperspectral observations for dust retrieval are that they can provide multiple atmospheric window channels that are most sensitive to dust aerosols and less sensitive to atmospheric gas absorption (Peyridieu et al., 2010; Capelle et al., 2018; Capelle et al., 2014; Peyridieu et al., 2013). On the other hand, these algorithms have two major limitations. First, the altitude of a dust layer and, therefore, its temperature profile affect the outgoing TIR radiance at TOA with a similar magnitude as DAOD (Pierangelo et al., 2004). As a result, dust altitude must be part of the state vector to be
105   retrieved together with DAOD in a stand-alone hyperspectral TIR dust retrieval algorithm, which makes retrieving dust particle size from limited information contents highly challenging (Pierangelo et al., 2005). Second, the relatively large footprint of hyperspectral sounders (~15 km) makes cloud masking and clearing a daunting task. As a result, the retrieval results are prone to cloud contamination (Song et al. 2018, Zheng et al. 2022).

110   A recent study by Zheng et al. (2022) (hereafter referred to as Z22) opened a new avenue for TIR-based dust retrievals by retrieving ten years of TIR DAOD at 5-km resolution over the global oceans based on combined CALIOP and Infrared Imaging Radiometer (IIR, a collocated higher-spatial-resolution TIR imager) observations. Both CALIOP

and IIR are onboard the CALIPSO satellite. The smaller (compared to AIRS and IASI) footprint size of IIR and the collocated CALIOP lidar make cloud masking much easier and more reliable than stand-alone hyperspectral algorithms. Moreover, the highly detailed and accurate dust vertical distribution provided by CALIOP not only makes the TIR DAOD retrieval more straightforward and accurate, but also allows for additional retrievals on dust particle size. Lastly, the collocated CALIOP Lidar also provides estimated $DAOD_{VIS}$, which opens potential applications for the observational synergistic VIS and TIR DAOD. Furthermore, unlike the passive VIS-NIR observations that are available at the daytime only, the combined VIS Lidar and TIR observations are also accessible at night, which allows further applications for investigating the diurnal variability of dust properties (Yu, Y. et al., 2021; Chédin et al., 2020). However, Z22 found that an accurate radiative closure between the simulated TIR radiance and observed TIR radiance for clear sky backgrounds is only possible for nighttime observations as there is an unresolved bias at daytime. In addition, because it used a single-band (i.e., the 10.6 µm IIR band) retrieval method, the algorithm allows for retrieving DAOD only.

To overcome the limitations in Z22 and further advance the TIR dust retrievals for coarse-mode dust size, in this study, instead of IIR, we use three MODIS TIR window bands (centred at 8.55 µm, 11.02 µm and 12.03 µm) for dust retrievals for the following reasons. The detector noise of MODIS in warm scenes (e.g., dust-laden sky) is 0.02-0.03 K, which is lower than that of IIR at 0.1-0.15 K (Madhavan et al., 2016). As a result, we can achieve a better radiative closure between radiative transfer simulation and MODIS observations in the clear sky, a premise for TIR-based dust retrieval, at all three TIR channels in both daytime and nighttime (details in Section 2.3). It first allows us to adopt the split-window technique (Zhang et al., 2006; Paepe and Dewitte, 2009) to reduce retrieval uncertainties compared with Z22 (detailed in Section 5.1). Moreover, by leveraging the information contents from all three bands, we can retrieve not only DAOD at 11 µm, further scaled to 10 µm (referred to as "$DAOD_{10µm}$"), but also the dust particle size represented by effective diameter (referred to as "D_{eff}"). Lastly, the daytime retrievals enable comparisons with VIS-NIR-based retrievals, such as MODIS, CALIOP and AERONET.

In the rest of the article, we introduce the collocated MODIS and CALIOP observation and the radiative transfer model in section 2. The implementation of the retrieval algorithm is detailed in section 3. Section 4 demonstrates the $DAOD_{10µm}$ and D_{eff} retrievals of three dust cases observed at Cape Verde and in the Caribbean Sea and compares them with ground-based and in-situ airborne measurements. Section 5 presents the climatological analysis of five-year retrievals of $DAOD_{10µm}$ compared with Z22 IIR-based and IASI-based retrievals and D_{eff} in terms of the seasonal and regional variation from 2013 to 2017. The discussions and conclusions are summarized in section 6.

2 Data and model

2.1 MODIS and CALIOP observations

In this study, dust properties, namely $DAOD_{10µm}$ and D_{eff}, are retrieved from collocated Aqua-MODIS and CALIOP observations. MODIS onboard the Aqua satellite, as a member of the A-train constellation, provides observations from 36 spectral bands ranging from VIS to TIR with near-daily global coverage and relatively high spatial resolution

(i.e., 250 m to 1 km at nadir). MODIS is equipped with onboard calibrators that enable stable calibration uncertainties
150   within ± 0.03 K for TIR bands (Xiong et al., 2009). This study primarily uses the MODIS Level-1B calibrated
upwelling radiances at TOA at three TIR spectral bands centered at 8.55 μm, 11.02 μm and 12.03 μm, respectively.
The TIR "window" bands mostly avoid contaminations from atmospheric gas absorptions and are sensitive to dust
optical properties in different orders (Z22). For better interpretation, the calibrated radiances are further converted to
equivalent brightness temperature (BT) computed based on Planck's law, and the corresponding spectral response
155   functions at the three selected TIR bands (see Figure 4b (black dash lines) in Section 3.2).

CALIPSO, launched in 2006, has also been a member of the A-train constellation that shares a similar and tightly
controlled Sun-synchronous polar orbit with Aqua MODIS until August 2018. CALIOP aboard CALIPSO is a two-
wavelength (532 and 1064 nm) polarization-sensitive Lidar with three receiver channels (one measuring the 1064 nm
160   backscatter intensity and two measuring orthogonally polarized components of the 532 nm backscatter). Unlike Aqua
MODIS, CALIOP has a much smaller spatial coverage due to its narrow cross-track footprint of around 70 m in
diameter. However, the 333-m along-track footprint with 30-to-60-m vertical resolution allows CALIOP to provide
detailed vertical structures of aerosols and clouds (Winker et al., 2009).

165   In this study, the dust contribution to a vertical column of attenuated backscatter is needed as we focus on retrieving
dust. Although the CALIOP operational aerosol product (i.e., the Vertical Feature Mask (VFM) product) determines
the aerosol sub-type for each aerosol layer (Kim et al., 2018), it does not provide the quantitative dust backscatter
profile for dust and non-dust aerosols mixed in the column. Therefore, we apply the estimated particulate
depolarization ratio (DPR) profile along with the total attenuated backscatter profile from the Version-4 Level-2
170   CALIOP aerosol profile product ("LID_L2_05kmAPro-Standard-V4" (Liu et al., 2019)) to derive the dust aerosol's
vertical distribution for $DAOD_{10\mu m}$ and D_{eff} retrieval. The VFM product is further used for filtering out the mis-
included non-dust aerosol profiles (see Appendix B for detail).

2.2 AMSR-E and MERRA-2 auxiliary data

The surface characteristics (i.e., surface emissivity and temperature) and the atmospheric profiles (i.e., temperature T,
175   pressure P, water vapor Qv and ozone O_3) are crucial for obtaining an accurate radiative transfer simulation in TIR at
TOA (Scott and Chedin, 1981). Unlike the hyperspectral observations with the capability to retrieve the instantaneous
atmospheric states, our retrieval requires inputs of these auxiliary data from third-party sources.

The atmospheric profiles T, P, Qv and O_3, are obtained from Version 2 Modern-Era Retrospective analysis for
180   Research and Applications (MERRA-2) assimilated products (Gelaro et al., 2017). Specifically, The MERRA-2
"inst3_3d_asm_Nv" product provides 3-hourly instantaneous atmospheric profiles at 72 pressure levels with a gridded
horizontal resolution of 0.625° longitude by 0.5° latitude. Detailed information can be found in Gelaro et al. (2017).
To assign the gridded MERRA-2 data to the simulations for the collocated MODIS and CALIOP (referred to as

"MODIS-CALIOP") observations, we first obtain the geolocation and time of all grid cells of MERRA-2 data. Then,

185   we find the spatially and temporally closest grid cell with each MODIS-CALIOP pixel.

As the retrieval is implemented over oceans only, which is explained in Section 2.3, we obtain the level-2 sea surface temperature (SST) retrieved based on the Advanced Microwave Scanning Radiometer - Earth Observing System Sensor (AMSR-E) onboard Aqua (ceased operation in December 2011), and its successor (launched in May 2012),

190   the Advanced Microwave Scanning Radiometer 2 (AMSR2) onboard GCOM-W1 that follows Aqua's orbit. The 6.9-GHz and 10.7-GHz channels from AMSR-E and AMSR2 are used for SST retrieval (Wentz and Meissner, 2000). Previous studies demonstrated that the SST retrievals over heavy dust-loading regions using TIR observations are underestimated due to the radiative impact of dust (Luo et al., 2019). However, microwave radiation has mostly no interaction with dust and, therefore, can avoid dust impacts and achieve better SST retrieval accuracy over dusty

195   regions (O'carroll et al., 2019). In this study, the SST at 56 km resolution from AMSR-E and AMSR-2 is collocated with MODIS-CALIOP. For the surface emissivity, we use the emissivity models (listed in Table 1) provided in version-2 Community Radiative Transfer Model (CRTM) (Van Delst, 2011), which is described in Section 2.3.

Finally, for each MODIS-CALIOP observation, the collocated MERRA-2 atmospheric profiles, AMSR-E/AMSR2

200   SST, and the internal surface emissivity model are used as the input for the radiative transfer simulation. All the satellite products, variables and auxiliary data are listed in Table 1.

Table 1: Values of variables from multi-source satellite sensors and auxiliary datasets that are used in this study

Satellite sensors	Product names	Variable names	Value is used
MODIS	MYD021KM (CloudSat_MODIS_AUX)	EV_1KM_Emissive	Radiances (BTs) at 8.5 μm, 11μm, 12μm
	MYD06 (CloudSat_MOD06_AUX)	Cloud_Phase_Optical_Properties (For daytime)	Clear (0)
		Viewing zenith angle	All
CALIOP	LID_L2_05kmAPro-Standard-V4-20	CAD_score	-100 to -90
		Particulate_Depolarization_Ratio_Profile_532	All
		Extinction_QC_Flag_532	0,1,16,18
		Total_Backscatter_Coefficient_532	All
		Atmospheric_Volume_Description	Three dust subtypes (dust, polluted dust, dusty marine)
	CAL_IIR_L2_Track-Standard-V4-20	Was_Cleared_Flag_1km	No single-shot cloud (0)
		TGeotype	Open Water (1700)
AMSR-E AMSR2	AMSR_E_L2_Ocean RSS_AMSR2_ocean_L3_daily	SST (sea surface temperature)	All

Auxiliary data	Product names	Variable names	Value is used
MERRA-2	Inst3_3d_asm_Nv	H, P, T, QV, O3	All
CRTMv2.3	Nalli.IRwater.EmisCoeff	Surface emissivity	All

205 **2.3 The radiative transfer models**

The foundation of a LUT-based retrieval method is an accurate radiative transfer model. For the radiative transfer simulation of terrestrial TIR radiation under clear atmospheric conditions, atmospheric gaseous absorption is critical. In this study, we use the version-2 CRTM developed by the US Joint Center for satellite data Assimilation (JCSDA) as the foothold for our retrieval (Chen et al., 2012; Han, 2006). The transmittance coefficients in CRTM are first
210 trained by applying regression algorithms to the line-by-line integrated transmittances for numerous atmospheric profiles (McMillin et al., 2006). Afterward, the gaseous absorption component can achieve an accuracy as high as the line-by-line transmittance but consumes far less computational time (Ding et al., 2011). As CRTM also supports MODIS's sensor coefficients, it is an optimal tool for simulating the atmospheric gaseous absorptions at the three selected MODIS TIR bands for our retrieval (Liang et al., 2016; Wang et al., 2016).

215

Although it is straightforward to use CRTM to handle the gas absorptions in the TIR, we found it difficult to use it to handle the scattering and absorption of dust due to the configuration and structure of the code. In this study, we use the Discrete Ordinate Radiative Transfer code (DISORT) to handle the dust aerosol scattering and absorption calculation (Stamnes et al., 1988). To combine CRTM and DISORT, we first use CRTM to simulate atmospheric
220 gaseous absorptions (output as the atmospheric optical depth) with input MERRA-2 atmospheric profiles. Afterward, the CRTM-simulated atmospheric optical depth with and without the vertical distribution of dust optical properties served as inputs for DISORT to simulate cloud-free dust-laden BTs and cloud-free clean (i.e., cloud-free and aerosol-free) BTs at the three MODIS TIR bands at TOA, respectively.

225 Prior to implementing the retrieval, the uncertainties contributed by the auxiliary data, the radiative transfer simulation, and the observational errors must be evaluated. Thus, we conduct the radiative closure benchmark between the CRTM-DISORT calculated and the MODIS-observed BTs under cloud-free and clean (without dust) conditions, which is detailly presented in Appendix A. Given that the error of the radiative closure benchmark over land and polar regions can reach up to 10 K due to the uncertainties from the assumed surface emissivity and temperatures (Z22), this study
230 focuses on retrievals over oceans within 60°S and 60°N only.

3 Description of the retrieval algorithm

In this section, we detailly describe the retrieval algorithm that is summarized in Figure 1, covering the collocation of MODIS and CALIOP observations and the process of cloud masking and dust detection, the *a priori* dust properties, 235   and the design of the LUT method and the uncertainty estimation.
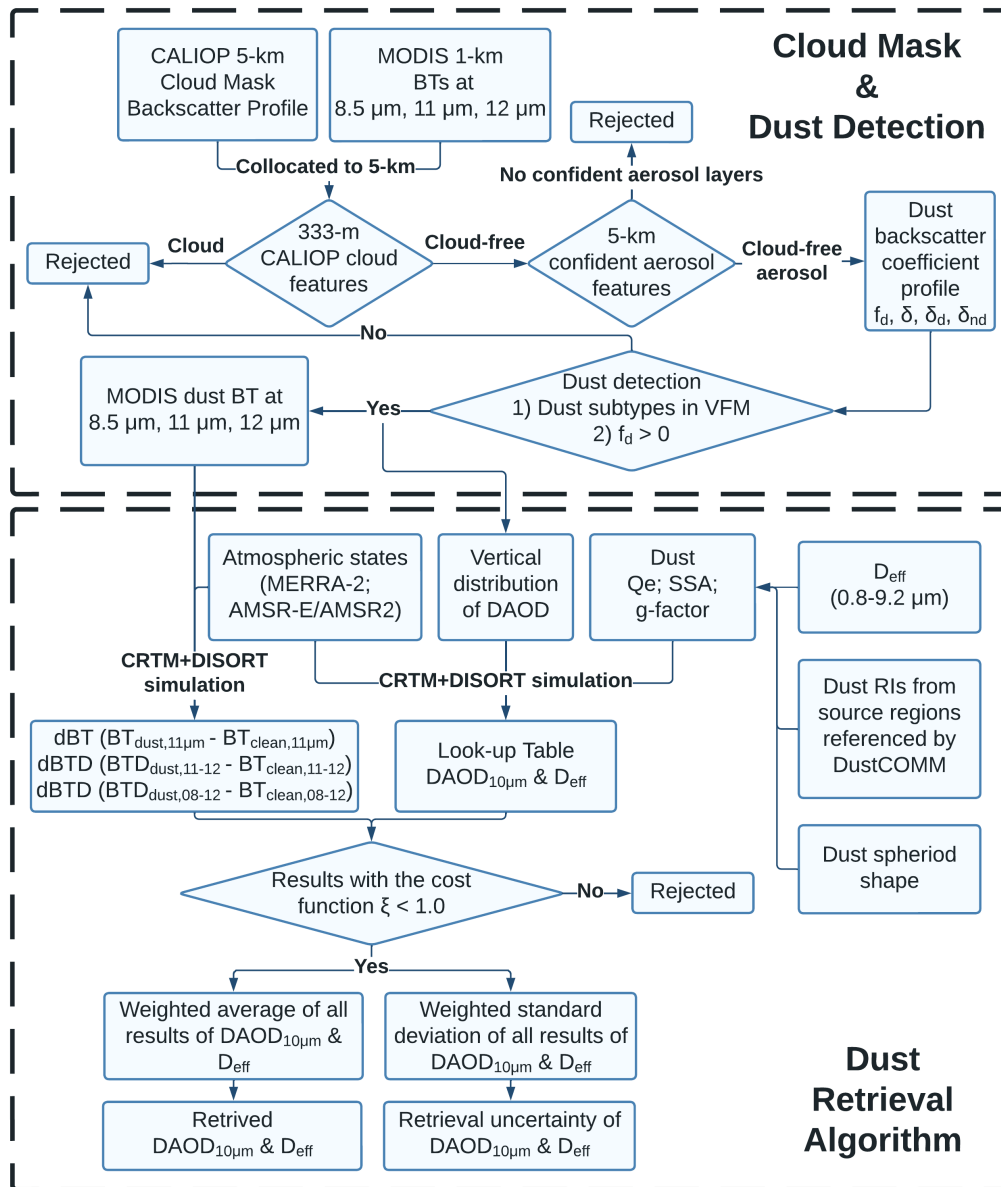

Figure 1: The flow chart of the retrieval process of $DAOD_{10\mu m}$ and D_{eff} using collocated MODIS-CALIOP observations.

240   The first step of the retrieval is to identify high-quality cloud-free dust-laden observations. Due to the different spatial coverage of MODIS and CALIOP, the retrieval requires collocated data from both sensors. The collocation process and the following cloud masking and dust detection and vertical distribution processing are similar to Z22 and are presented in detail in Appendix B.

3.1 *A priori* dust properties

In addition to the vertical distribution, the retrieval needs to assume dust bulk optical properties. In this section, we
245   introduce the dust PSD, dust shapes, and dust RI that are used to calculate the bulk optical properties (i.e., the extinction efficiency (Q_{ext}), single scattering albedo (SSA) and asymmetry factor (g-factor)).

3.1.1 Monomodal dust coarse-mode particle size distribution

Dust PSD is commonly presented by a two-mode (i.e., fine mode ($D_p < 1.0$ µm) and coarse mode ($D_p > 1.0$ µm)) lognormal size distribution (Dubovik et al., 2002). As the fine mode dust has a negligible effect on TIR observation,
250   we assume a normalized (i.e., total volume concentration equals unity) monomodal lognormal volume size distribution to represent the coarse-mode dust PSD, which is defined as

$$\frac{dV}{dlnD} = \frac{1}{\sqrt{2\pi}\sigma} \exp\left[-\frac{ln^2\,(D/D_m)}{2\sigma^2}\right] \qquad (1)$$

where D is the volume-equivalent sphere geometric diameter for spheroidal dust particle assumption (see Section 3.1.2), D_m is the geometric volume median diameter, $\frac{dV}{dlnD}$ is the volume PSD, and σ is the standard deviation. Note
255   that the sensitivity of σ to the TIR radiative signature at TOA is negligible compared with that of AOD and D_m (Pierangelo et al., 2005) (see Figure S5). Therefore, to simplify the retrieval, we first set $\sigma = 0.7$ (i.e., ln(2.0)) as it is a good representation for the coarse-mode dust PSDs in both in-situ measurements and satellite retrievals (Capelle et al., 2018; Ryder et al., 2018). We further use the effective diameter defined by Hansen and Travis (1974) to represent the monomodal PSDs with dependence on D_m as

260    $$D_{eff} = \frac{\int_0^\infty D^3 n(D) dD}{\int_0^\infty D^2 n(D) dD} \qquad (2)$$

where $n(D)$ is the dust number concentration converted by the volume distribution with $\sigma = 0.7$ and varied D_m.

Note that in-situ measurements of dust PSD show that the coarsest record of dust particles over the transport regions (i.e., over oceans) was measured during the Fennec campaign in June 2011 (Ryder et al., 2013a), with an estimated
265   D_m at around 10.0 µm. Therefore, for the retrieval, we define the minimum and maximum dust coarse-mode PSDs with their representations of D_m from 1 µm to 12 µm and D_{eff} from 0.8 µm to 9.2 µm, (see Figure S1). Dust PSDs within this range are used for calculating the dust bulk optical properties as inputs for building the LUT of $DAOD_{10µm}$ and D_{eff}.

9

3.1.2 Dust refractive indices and dust shape

270   The RI of dust, determined by dust mineral compositions, has a profound impact on dust scattering properties and therefore the retrieval results (Sokolik and Toon, 1999). Ideally, the dust RI should be retrieved simultaneously with other properties of dust. However, given the highly limited information content from the three MODIS TIR bands, a retrieval of dust RI is not possible, at least in this study. It should be noted that most previous studies also used pre-assumed dust RI, often one or two simple global constants, in their retrievals including widely used operational aerosol

275   retrieval products (Capelle et al., 2018; Zhou et al., 2020).

Nevertheless, in this study, we try to incorporate the spatial variability of dust RI in our retrieval by using two newly developed datasets. One is a state-of-the-art dust RI database developed by Di Biagio et al. (2017) (referred to as the "Di-Biagio RI"), which provides dust RIs retrieved based on surface soil samples collected in nineteen arid and semi-

280   arid sites from worldwide dust source regions. The Di-Biagio RI database provides the observational basis for accounting for the regional dependence of dust RI. The other is the fractional contribution over oceans supplied by various dust source regions from the DustCOMM-2021 dataset developed by Kok et al. (2021a), which is used to assign dust RIs from different source regions to the observed dust aerosol over oceans. Details of the dust RI assignments are presented in Appendix C.

285

Dust particles have irregular and non-spherical shapes, which vary greatly from case to case and from location to location (Scheuvens and Kandler, 2014). Using spherical assumptions for non-spherical dust in remote sensing would cause significant uncertainty (Huang et al., 2020; Dubovik et al., 2002; Nousiainen and Kandler, 2015). It is essential to adopt a quantified non-sphericity to represent dust optical properties better. However, characterizing the complex

290   morphology of dust particles remains challenging. Previous studies used different assumptions of dust particle shape to evaluate the sensitivity of dust optical properties to the morphology, such as spheroid (Dubovik et al., 2006), ellipsoid (Meng et al., 2010) and polyhedral (Liu et al., 2013).

The non-sphericity of the aspherical shape is often represented by the aspect ratio, defined as the ratio of the longest

295   particle dimension to the intermediate particle dimension. The higher the aspect ratio, the greater the non-sphericity. The spheroid shape assumption is a first-order approximation of dust non-sphericity (Mishchenko et al., 1997; Dubovik et al., 2002) and is widely used for non-spherical aerosol retrievals (Levy et al., 2013; Kahn et al., 2010). To seek a broader application of this study to others, we stick to the spheroid assumption with the size-independent aspect ratio distribution from Dubovik et al. (2006) for the retrieval. Nonetheless, the retrieval based on a more advanced

300   non-spherical dust optical properties database, such as the hexahedral shape (Saito et al., 2021), will be evaluated in future studies.

By assuming dust particles with spheroidal shape, we calculate the dust single-particle optical properties for each *a priori* dust RI using the T-matrix method (Mishchenko et al., 1996). Afterward, the bulk optical properties are

305   integrated according to the pre-assumed dust PSDs and aspect ratios of spheroidal dust.

3.2 The look-up table and the uncertainty estimation

The $DAOD_{10\mu m}$ and D_{eff} are retrieved from three MODIS TIR bands using a LUT method. To illustrate the LUT, we use CRTM-DISORT to simulate the cloud-free clean BT at 11 μm (referred to as "BT_{11}"), spectral BT differences (BTD) between 11 μm and 12 μm (referred to as "BTD_{11-12}") and that between 8.5 μm and 12 μm (referred to as

310 "BTD_{08-12}"), by giving a typical tropical atmospheric profile with a dust layer distributed at the mid-level troposphere (i.e., 2-6 km, see Figure S6). Afterward, with the *a priori* dust D_{eff}, dust RI, and dust spheroidal aspect ratios, the calculated dust bulk optical properties based on the T-matrix method can be used as inputs in CRTM-DISORT to simulate cloud-free dust BT_{11}, BTD_{11-12} and BTD_{08-12}. With the input DAOD at 11 μm ($DAOD_{11\mu m}$) ranging from 0.0 to 1.0 and D_{eff} ranging from 0.8 μm to 9.2 μm (see Figure S1 for corresponding dust PSDs), we build a LUT consisting

315 of BT_{11}, BTD_{8-12} and BTD_{11-12} as shown in Figure 2a. The assumed dust RI for the LUT is from Algeria in Northeast Africa. Example LUTs corresponding to other dust RIs are shown in Figures S7 and S8.

Considering the higher dust extinction signal expected at 10 μm compared to 11 μm (see Figure 2b and Pierangelo et al. (2004)), we scale $DAOD_{11\mu m}$ to $DAOD_{10\mu m}$ based on the Qe spectral behavior following $\frac{DAOD_{11\mu m}}{DAOD_{10\mu m}} = \frac{Qe_{11\mu m}}{Qe_{10\mu m}}$. As a

320 result, our final retrieval products contain $DAOD_{10\mu m}$ and D_{eff}.
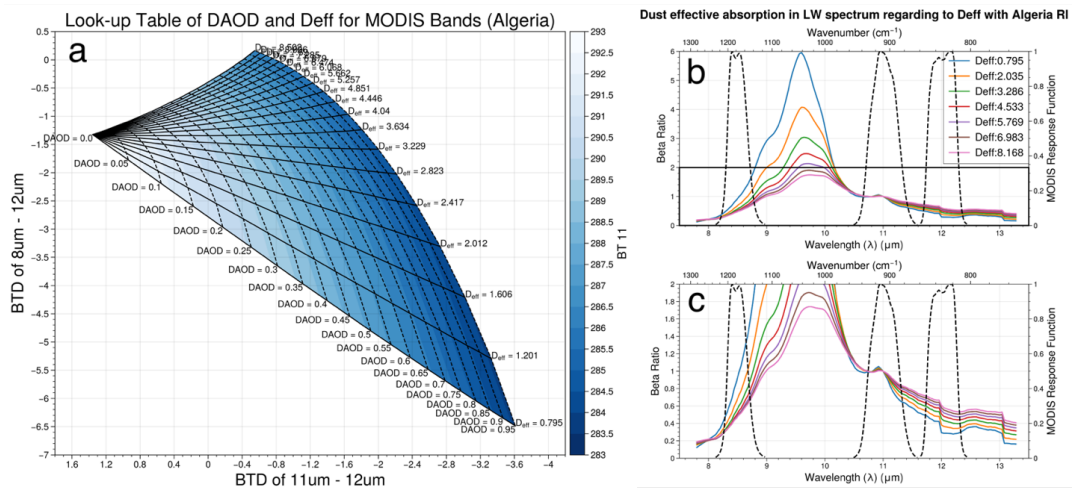
Figure 2: (a) The example of the LUT of BTD_{8-12} (y-axis), BTD_{11-12} (x-axis) and BT_{11} (colour-filled contours) corresponding
325 **to $DAOD_{11\mu m}$ ranging from 0.0 to 1.0 (dashed lines) and D_{eff} ranging from 0.8 μm to 8.2 μm (solid lines) and the Algeria dust RI from Di-Biagio Database. At the point of DAOD = 0.0, the BTD_{8-12} and BTD_{11-12} correspond to the cloud-free clean scenario. (b) The β-ratio to 11 μm calculated based on D_{eff} ranging from 0.8 μm to 8.2 μm and the Algeria dust RI within the TIR spectrum between 7.5 μm and 13.5 μm. (c) The zoom-in area of the black rectangle in (b).**

The variation of BTDs and BT_{11} with $DAOD_{11\mu m}$ and D_{eff} is determined by the dust Qe, SSA and g-factor at the three
330 TIR bands. To better understand the variations of BTDs in the LUT, we introduce the so-called β-ratio, defined as follows.

$$\beta(\lambda_1/\lambda_2) = \frac{Q_e(\lambda_1)[1-\omega(\lambda_1)g(\lambda_1)]}{Q_e(\lambda_2)[1-\omega(\lambda_2)g(\lambda_2)]} \qquad (3)$$

11

where Q_e is the extinction efficiency, ω is the SSA, and g is the asymmetry factor. The β-ratio was often used to represent the spectral difference of dust "effective absorption" (i.e., absorption and backward scattering) in the TIR

335 spectrum in many studies on dust, volcanic ash and ice cloud retrieval (Pavolonis et al., 2013; Pavolonis et al., 2015; Garnier et al., 2013). Because the variation of BT_{11} in Figure 2a serves as the single-band dust radiative signature, we present the β-ratio with respect to 11 μm (i.e., $\lambda_2 = 11\ \mu m$ in Eq.(3)) for varied D_{eff}, as shown in Figure 2b. The β-ratios for wavelength ranging from 12 μm to 11 μm over the whole range of the input D_{eff} are lower than one. It means that the dust "effective absorption" at 11 μm is always more significant than that at 12 μm, regardless of the size

340 variation. In contrast, the cloud-free clean BT at 11 μm is higher than that at 12 μm due to the less atmospheric absorptions at 11 μm as described in Appendix A. Consequently, in Figure 2a, the BTD_{11-12} decreases with increasing $DAOD_{11\mu m}$ regardless of how D_{eff} changes.

On the other hand, the BTD_{8-12} is more sensitive to D_{eff} than to DAOD. First, the cloud-free and clean BT at 8.5 μm

345 is similar to that at 12 μm due to similar gas absorption. However, the dust "effective absorption" at 8.5 μm is larger than that at 12 μm when D_{eff} is relatively small (e.g., 1.0 μm < D_{eff} < 3.0 μm) in Figure 2b, there are negative trends of BTD_{8-12} with increasing DAOD in Figure 2a. In contrast, in Figure 2b, the dust "effective absorption" at 8.5 μm is weaker than that at 12 μm when D_{eff} is relatively large (e.g., D_{eff} > 5.0 μm), leading to positive trends of BTD_{8-12} with increasing DAOD in Figure 2a. In between, the sensitivity of BTD_{8-12} to DAOD can be nearly zero when dust D_{eff} is

350 moderate (e.g., D_{eff} = 3.6 μm). As such, the radiative signature of DAOD and D_{eff} can be separated using BTD_{8-12} and BTD_{11-12}, allowing the simultaneous retrieval of both parameters based on the three MODIS TIR bands.

Besides the dust particle size (e.g., D_{eff}), dust "effective absorption" at the three TIR bands also depends on the LW dust RI. The dust RI directly changes the spectral behavior of the dust "effective absorption" and reshapes the LUT

355 of BTD_{8-12} and BTD_{11-12} (see Figures S7 and S8). Due to the limited observational signature, the retrieval of dust RI is unachievable in this study. The retrieval uncertainty associated with the assumption of dust RI thus needs to be assessed. In addition, the errors resulting from radiance observation itself and radiative transfer modeling (Figure A1 in Appendix A) also need to be factored in.

360 We implement the retrieval algorithm in three steps to find an optimal retrieval with the assessed uncertainties. Firstly, we define a cost function ξ of the normalized distance between the simulated BT and BTDs in the LUT and the observed BT and BTDs as

$$\xi(DAOD, Deff) = \frac{1}{3}\left[\frac{\left(BT_{11}^{sim}-BT_{11}^{obs}\right)^2}{\sigma_{11}^2} + \frac{\left(BTD_{11-12}^{sim}-BTD_{11-12}^{obs}\right)^2}{\sigma_{11-12}^2} + \frac{\left(BTD_{8-12}^{sim}-BTD_{8-12}^{obs}\right)^2}{\sigma_{8-12}^2}\right] \qquad (4)$$

The subscript of *11,11-12* and *8-12* represents the BT at the 11μm band, BTD_{11-12} and BTD_{8-12}, respectively. The

365 superscript of *sim* and *obs* represents the BT or BTD obtained by simulations and observations, respectively. The σ represents the standard deviation of the uncertainty assessed through the clear-sky radiative closure (see Figure A1), which represents the summation of errors from the observation and simulation using *a priori* atmosphere states. The first term on the right-hand-side of Eq. (4) represents the normalized distance between the observed and the simulated

BT at the 11μm band. The second and the last term represents the summation of the normalized distance between the
370   observed and the simulated BTD$_{11-12}$ and BTD$_{8-12}$, respectively.

Secondly, by using Eq. (4), we acquire a solution when the normalized distance is within the range of the evaluated
uncertainty ($\xi < 1$). In addition, as mentioned in Appendix C, each observation would possibly assume more than
one dust RI for retrieval. Therefore, we build multiple LUTs corresponding to multiple RIs and implement the retrieval
375   with all of them. All the solutions that satisfy $\xi < 1$ in these LUTs are collected.

Finally, the optimal retrieval results of DAOD and D$_{eff}$ are defined as the average of the collected solutions
corresponding to multiple *a priori* dust RIs weighted by their corresponding cost function ξ as $w = 1 - \xi$. The
weighted standard deviation thus represents the estimated retrieval uncertainty as

$$S_w = \sqrt{\sum_{i=1}^{N} w_i (x_i - \overline{x_w})^2 / (N-1) \frac{\sum_{i=1}^{N} w_i}{N}} \qquad (5)$$

380

where x_i is the ith solution of DAOD or D$_{eff}$, w_i is the weight of ξ for the ith solution, N is the number of non-zero
weights, and $\overline{x_w}$ is the weighted mean of the collected solutions (Heckert and Filliben, 2003; Hao and Mendel, 2013).
In this step, the uncertainties associated with the assumptions of *a priori* dust RI and the clear-sky radiative closure
are taken into account by the weighted average and the weighted standard deviation.

385

After the retrieval, the quality assurance (QA) flag is assigned as 0 for successfully retrieved results. The retrieval
with less than two solutions satisfying $\xi < 1$ is rejected and is assigned with QA flag as 1. By implementing the
retrieval for the five-year MODIS-CALIOP observations from 2013 to 2017, which will be analyzed in detail in
Section 5, we present the seasonal distribution of cloud-free dust samples (N_{dust}), successfully retrieved dust samples
390   ($N_{retrieval}$; QA flag = 0), and the retrieval success rate ($N_{retrieval} / N_{dust}$), which reaches to 90%-100% over dust transport
regions, as shown in Figure S9.

In summary (Figure 1), we obtain the cloud-free dust aerosol vertical profiles using the CALIOP cloud mask, dust
detection and vertical-scaling method introduced in Appendix B. Afterward, the *a priori* dust properties presented in
395   Section 3.1 serve as inputs for CRTM-DISORT to build the LUT of DAOD and D$_{eff}$. Lastly, we retrieve DAOD$_{11μm}$
further scaled to DAOD$_{10μm}$ and D$_{eff}$ by averaging the solutions that satisfy $\xi < 1$ weighted by ξ and estimate the
corresponding retrieval uncertainty based on the corresponding ξ-weighted standard deviation.

4 Evaluation of CALIOP-MODIS retrievals with in-situ measurements – case studies

400   ### 4.1 A case study for transported Saharan dusts over Cape Verde in summer

In this section, we implement the retrieval to a dust plume originating from North Africa and being transported over
the North Atlantic on August 16th, 2015. We use this case to evaluate the retrieved DAOD$_{10μm}$ and D$_{eff}$ through

comparisons with the in-situ measured dust particle size and the collocated AERONET (Aerosol Robotic NETwork) measurements

405   **4.1.1 Evaluation of retrieved DAOD$_{10\mu m}$**

Figure 3a shows the total attenuated backscatter at 532 nm from CALIOP for the dust case observed on August 16th, as shown from left (South) to right (North) with the geolocation highlighted in the upper left sub-panel. The CALIOP orbit passed nearby Cape Verde (16.733°N, 22.935°W) around 03:34 UTC with nighttime observations for the dust plume. Figure 3b shows the corresponding spatial variation of total AOD$_{532nm}$ (blue dots) and DAOD$_{532nm}$ (red dots)

410   estimated with a Lidar ratio of 44 sr and uncertainty of ±10 sr as described in Appendix B. The mean DAOD$_{532nm}$ (1.1) is ~83% to the mean total AOD$_{532nm}$ (1.33), indicating that "pure" dust aerosols dominate this offshore dust plume. Therefore, as a "golden standard", the measured AERONET AOD at Cape Verde for this dust plume can be approximated as DAOD to assess the CALIOP DAOD and the corresponding retrieved DAOD$_{10\mu m}$. Unfortunately, although AERONET at Cape Verde observed a maximum AOD event at 18:10 on Aug 16^{th,} as shown in Figure 3d, it

415   does not provide any nighttime measurement for this case.
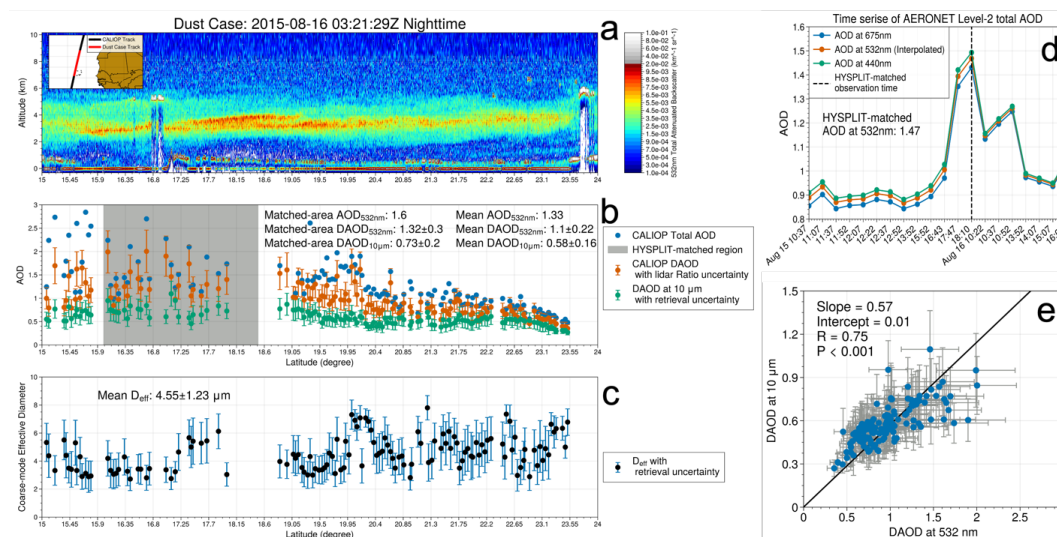
Figure 3: The nighttime case on August 16th, 2015. (a) The CALIOP total attenuated backscatter at 532 nm on August 16th, 2015, over the downwind region of the Sahara Desert (the orbit at upper left). (b) The CALIOP total AOD (blue

420   **dots), CALIOP DAOD (red dots), and the retrieved DAOD$_{10\mu m}$ (green dots) of the cloud-free dust-laden profiles. The gray shadow area represents the part of the dust plume (16°N-18°N) observed by CALIOP that is matched with the AERONET measurement based on the HYSPLIT back trajectories as shown in Figure 4 (c) The retrieved D$_{eff}$ (black dots) of the cloud-free dust-laden profiles with the estimated uncertainty (cyan error bars). (d) The time series of the AERONET level-2 AOD at 675 nm (blue dot line), 440 nm (green dot line) and 532 nm (orange dot line, interpolated) at**

425   **AERONET Cape Verde from 08-15-2015 to 08-16-2015. The black dash lines indicate the time that AERONET measured the same dust plume observed by CALIOP later, proven by the HYSPLIT back trajectories as shown in Figure 4. (e) The**

scatter plot of $DAOD_{10\mu m}$ versus $DAOD_{532nm}$ for the whole dust case. The grey error bars represent the uncertainties of $DAOD_{10\mu m}$ (vertical) and $DAOD_{532nm}$ (horizontal). The black line represents the robust linear regression with correlation coefficient (R), slope, intercepts, and p-value (P).

430

Due to the different observation times and locations between CALIOP and AERONET, to compare their AODs, we present the ensemble back trajectories simulated by the Hybrid Single-Particle Lagrangian Integrated Trajectory (HYSPLIT) model (Stein et al., 2015) from the passing-by times of the MODIS-CALIOP orbits and the AERONET Cape Verde as shown in Figure 4. Note that the vertical distribution of the dust plume is concentrated around 3 km to

435   4 km (see Figure 3a). Therefore, the HYSPLIT back trajectories are initiated at 3 km and 4 km. In Figure 4a, the HYSPLIT back trajectories of CALIOP between 16°N to 18°N show that the dust plume was seen by AERONET Cape Verde at 18:10 on Aug 15th (see Figure 4b). Bearing in mind that the AOD of the dust plume may change after the the 10-hour transport from AERONET Cape Verde to the CALIOP orbit track, we found that the CALIOP $DAOD_{532nm}$ (1.32 ± 0.3 averaged from 16°N to 18°N, Figure 3b) is consistent with the AERONET AOD_{532nm}

440   (interpolated, Figure 3d) of 1.47 within its uncertainty.

In addition, both back trajectories from CALIOP (including trajectories > 18°N) and AERONET show similar transport patterns from east to west with initial emission (i.e., back trajectories' height reaches 0 km in Figure 4b) from the source regions (black dash regions in Figure 4a) in Algeria and Mali in both horizontal and vertical view.

445   Thus, we can assign the Di-Biagio RIs from Algeria and Mali as the *a priori* dust RI for retrieval. The retrieved $DAOD_{10\mu m}$ (green dots in Figure 3b) shows a reasonable correlation with $DAOD_{532nm}$ (R = 0.75 in Figure 3e). Because of the spectral difference between TIR and VIS, the HYSPLIT-matched mean $DAOD_{10\mu m}$ (0.73) is ~55% of the value of $DAOD_{532nm}$ (1.32). For the entire case, $DAOD_{10\mu m}$ is ~57% (k = 0.57 in Figure 3e) of $DAOD_{532nm}$. Note that both ratios are within the empirical range of the TIR-to-VIS DAOD ratio from 28% to 65% (Peyridieu et al., 2013),

450   depending on the assumptions of dust PSD, dust RI and dust non-spherical shape.
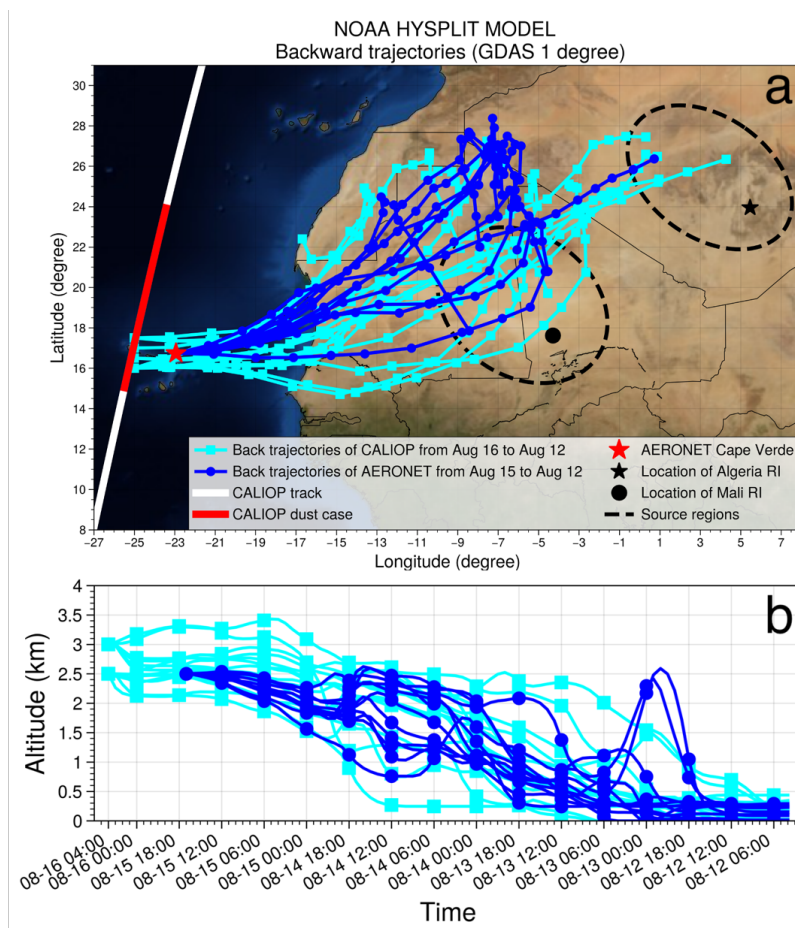
Figure 4: The distribution of the spatial (a) and the vertical (b) ensemble HYSPLIT back trajectories on the CALIOP dust case on 08-16-2015 (cyan rectangle solid lines) and the AERONET Cape Verde observation for the dust case on 08-15-2015 (blue dot solid lines). The black star and circle represent the geolocation of Di-Biagio RI collected over Algeria and Mali, respectively. The red star denotes the geolocation of the AERONET Cape Verde site.

4.1.2 Comparison of D_{eff} with AER-D in-situ measurements

In this section, we evaluate the D_{eff} retrieval by comparing the D_{eff}-corresponding monomodal PSD with those deduced from the lognormal-fitted dust PSD measured during the AERosol Properties – Dust (AER-D) campaign from Aug 7th to Aug 25th, 2015, over the outflow region of North Africa around Cape Verde (Ryder et al., 2018). We also compared with the AERONET-version-3 Level-2 two-mode PSD (referred to as "AERONET PSD") on Aug 16th at Cape Verde (Dubovik et al., 2006) (see Figure 5b). The AER-D campaign provides measured dust PSD and the corresponding uncertainty for dust within the Sahara Air Layer (SAL) (see Figure 5a) and in the marine boundary layer from various airborne instruments (Ryder et al., 2018). In this case, as the CALIOP-observed dust plume is well

465   confined within 2-5 km (Figure 3a), we choose the AER-D SAL campaign mean log-fit size distribution (referred to
as "AER-D PSD"), which is measured within 1.2-4.8 km (Ryder et al., 2018), in our comparison.
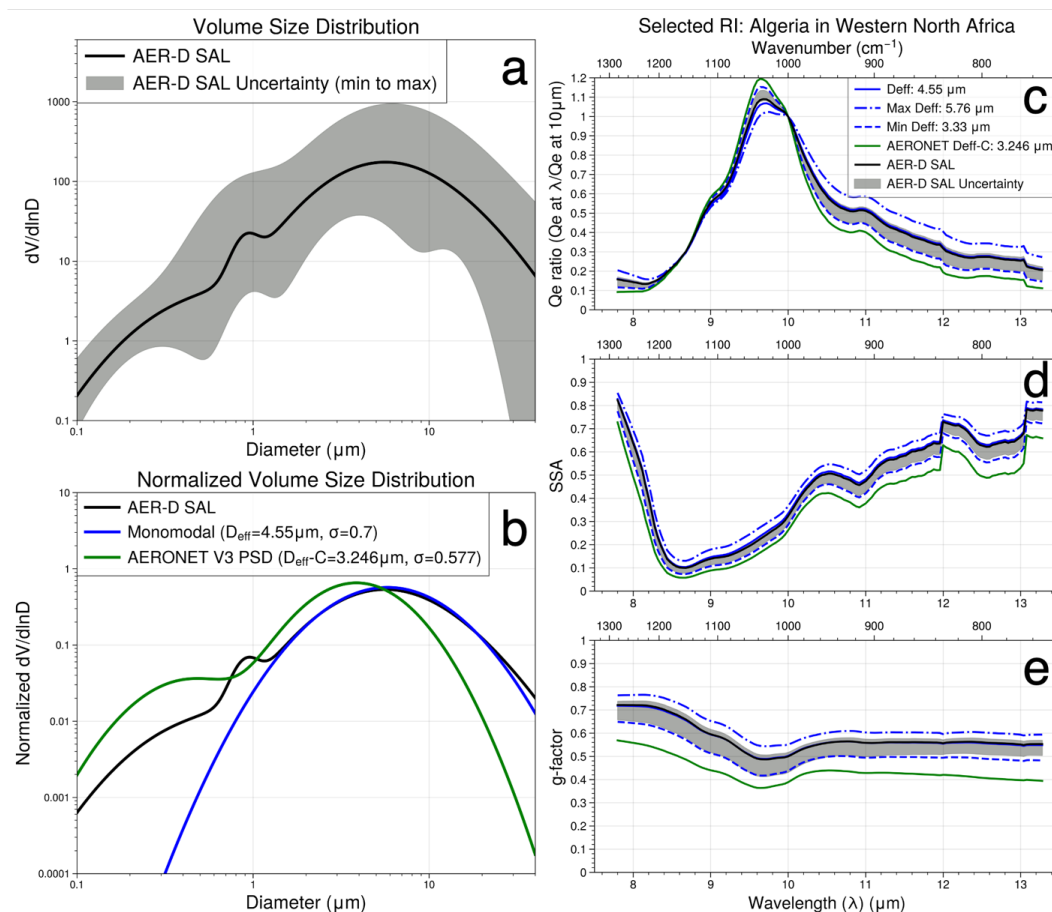
Figure 5: (a) The volume lognormal (*dVdlnD*) AER-D PSD (black) with gray shadow area indicating the min-to-max range
470   **of the measurement uncertainty obtained from Ryder et al. (2018). (b) The normalized *dVdlnD* of AER-D (black), the**
retrieved coarse mode PSD corresponding to D_{eff} = 4.55 μm (blue) and the AERONET PSD (green). (c-e) The Qe ratio to
10 μm (c), SSA (d), g-factor (e) calculated based on the AER-D PSD (black) with min-to-max uncertainty (grey shadow),
retrieved coarse mode PSD (blue) with the retrieval uncertainty (blue dash curve for the lower bound; blue dash-dot curve
for the upper bound) and AERONET PSD (green).

475

Figure 3c shows the retrieved D_{eff} for the dust case. We found that the spatial variation of D_{eff} is generally positively
correlated with that of $DAOD_{10μm}$ and with a mean value of 4.55 μm with the uncertainty ranging from 3.33 μm to
5.76 μm. Therefore, we obtain the monomodal PSD corresponding to D_{eff} = 4.55 μm to compare with the normalized
AER-D PSD and the AERONET PSD. In Figure 5b, the AEROENT-retrieved coarse mode PSD is systematically

480   smaller than that of AER-D, while the monomodal PSD with $D_{eff} = 4.55$ μm agrees well with the AER-D coarse mode PSD, although the fine mode of AER-D PSD is not compared because not relevant for LW.

For a perhaps more relevant comparison of the three PSDs in coarse mode, we compare their corresponding optical properties, namely the dust Qe ratio at 10μm, SSA and g-factor in the TIR spectrum ranging from 8 μm to 13 μm (See

485   Figures 5c to 5e). The reason for using the dust Qe ratio at 10 μm is that the retrieved $DAOD_{10μm}$ provides a constraint of dust extinction at 10 μm, while the dust PSD further determines the spectral Qe ratio of other TIR wavelength to 10 μm. We found that the spectral Qe ratio, SSA and g-factor calculated based on the monomodal PSD used in our retrievals are consistent with that calculated based on AER-D PSD. It demonstrates that although our monomodal PSD lacks fine mode dust, the retrieved D_{eff} can still provide almost identical dust optical properties in TIR as the AER-D

490   PSD has based on the constraint from the retrieved $DAOD_{10μm}$. In other words, the combination of $DAOD_{10μm}$ and D_{eff} with comparable accuracy as in-situ measurements but better spatiotemporal coverage is a valuable tool for reducing the global mean LW dust DRE uncertainties due to DAOD and dust particle size.

On the other side, all three optical properties calculated based on the AERONET PSD are bias low compared with

495   that based on AER-D and the retrieved PSD. As the fine-mode PSD has a negligible impact on dust optical properties in TIR, the result suggests that the AERONET coarse-mode PSD is highly likely to be underestimated in terms of size, which has been pointed out in several studies comparing AERONET PSD with other in-situ measurements (Müller et al., 2010; Müller et al., 2012; Mcconnell et al., 2008; Adebiyi et al., 2023). Due to the difficulties of comparing the PSD from the column-integrated retrieval to that from the lofted-layer measurement (Toledano et al.,

500   2019), the possible reasons are as-of-yet not well-explained, which require detail investigations in the future.

### 4.2 Evaluation of D_{eff} with SAMUM-2 and SALTRACE in-situ measurements

Noting that limiting the validation of D_{eff} with one case may be biased. To better demonstrate the reliability of the D_{eff} retrieval, we compare the retrieved D_{eff} with in-situ measured dust PSDs from two additional field campaigns. One is from the second field experiment of the Saharan Mineral Dust Experiment project (SAMUM-2) in the Cape Verde

505   area during January to February 2008 (Weinzierl et al., 2011). The other is the Saharan Aerosol Long-Range Transport and Aerosol–Cloud-Interaction Experiment (SALTRACE) that is taken place over the North Africa, the Atlantic Ocean, and the Caribbean from June to July 2013 (Weinzierl et al., 2016).

4.2.1 Comparison of D_{eff} with SAMUM-2 – A case over Cape Verde in winter

To compare with the SAMUM-2 campaign, we perform the retrieval for a nighttime dust case observed eastward Cape

510   Verde on Jan 28, 2008, as shown in Figure 6. Figure 6a shows the dust case is a low-altitude-level case up to ~ 2 km, consistent with the dust sampling of the experimental flights on January 28th in SAMUM-2 (see Table 2 and Figure 9 in Weinzierl et al. (2011)). As shown in Figure 6b, the mean retrieved D_{eff} is 3.68 μm, which is further used to construct the corresponding PSD for the comparison with SAMUM-2 dust PSD (see Figure 6c). In this case, we implement the retrieval using the RI assignments introduced in Section 3.1.2 and Appendix C instead of performing HYSPLIT back

515   trajectories to identify dust source regions. In addition, this wintertime dust case has lower dust loading (not shown) than the summertime case in Section 4.1, leading to a lower information content for retrieving D_{eff} (see Figure 2a). Therefore, there is a mean retrieval uncertainty of 2.0 μm larger than the summertime case.
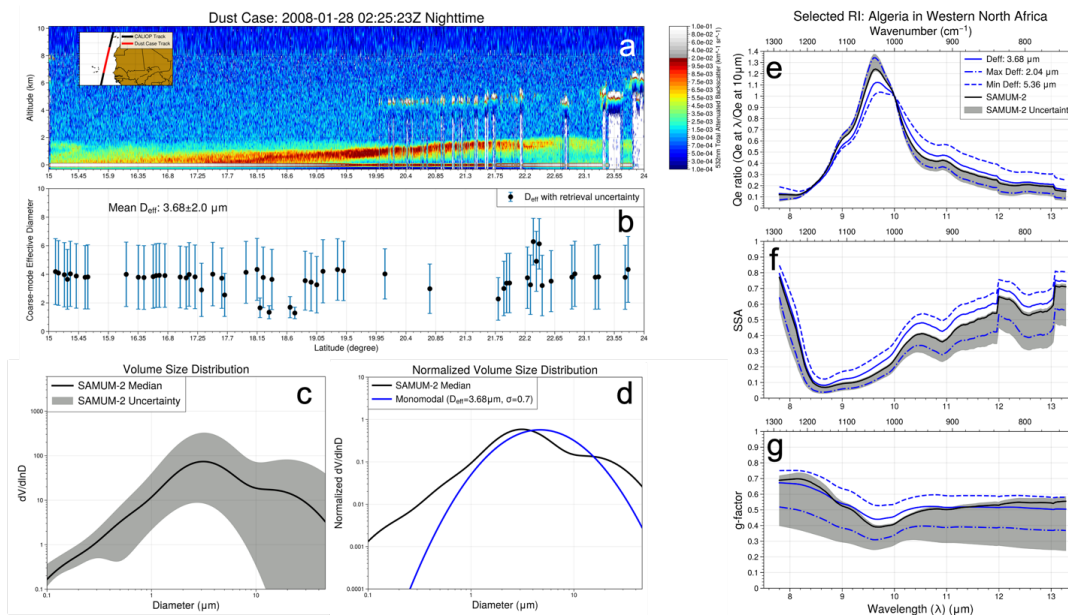
Figure 6: (a) The CALIOP total attenuated backscatter at 532 nm on January 28th, 2008, over the downwind region of the
520   **Sahara Desert (the orbit at upper left). (b) The retrieved D_{eff} (black dots) of the cloud-free dust-laden profiles with the retrieval uncertainty (cyan error bars). (c) The volume lognormal (*dVdlnD*) SAMUM-2 PSD (black) with gray shadow area indicating the range of the measurement value from 3- to 97- percentile obtained from Weinzierl et al. (2011). (d) The normalized *dVdlnD* of SAMUM-2 (black) and the retrieved coarse mode PSD corresponding to D_{eff} = 3.68 μm (blue). (e-g) The Qe ratio to 10 μm (e), SSA (f), g-factor (g) calculated based on the SAMUM-2 PSD (black) with its uncertainty (grey**
525   **area) and the retrieved coarse mode PSD (blue) with the retrieval uncertainty (blue dash curve for the lower bound; blue dash-dot curve for upper bound).**

In Figure 6d, we found that the monomodal PSD corresponding to the mean retrieved D_{eff} agrees with SAMUM-2 PSD by having the peak between the third and fourth modes of SAMUM-2 PSD. Due to the limitation of the fixed
530   assumption of the lognormal volume distribution's standard deviation, the monomodal PSD overestimates dust with D_p from 4 to 13 μm but underestimates dust with D_p > 13 μm. Because of that, the Qe ratio, SSA and g-factor corresponding to the monomodal PSD have slight differences from that of the SAMUM-2 PSD in the TIR spectral region. However, the dust TIR optical properties of the two PSDs are generally consistent after considering their uncertainties. It shows the D_{eff} retrieval's capability to capture the seasonal differences of dust size in the Cape Verde
535   area revealed by the AER-D and SAMUM-2 filed campaigns.

4.2.2 Comparison of D_eff with SALTRACE – A dust case transport throughout North Atlantic from June 12th to June 23rd, 2013

In order to evaluate the D_{eff} retrieval at long-range transport regions and demonstrate the variation of D_{eff} during the transport, we compare our results with the dust D_{eff} measured during the SALTRACE field experiment that studied a Lagrangian dust plume over both Cape Verde (SALTRACE-E) and Barbados (SALTRACE-W) on June 17th and June 22nd, 2013.

First of all, we perform the retrieval on a series of MODIS-CALIOP observations from June 16th within the Cape Verde area to June 23rd over the Caribbean Sea, as shown in Figure 7. In Figure 7a, the dust plume was vertically distributed between 2 km to 6 km, with the mean retrieved D_{eff} at 4.8 μm (Figure 7a2) on June 16th. From June 18th to 20th, the dust plume was transported to the mid-Atlantic (~43°W) and decreased the layer height from 2-5 km to 2-4 km (Figures 7b1 and 9c1). Meanwhile, the mean retrieved D_{eff} reduced from 4.3 μm to 4.0 μm (Figures 7b2 and 7c2). Figures 7d1 to 7f1 show that the dust plume traveled toward the Caribbean Sea from June 21st to June 23rd, maintaining the layer height between 1.5 km and 3.5 km and the retrieved D_{eff} at ~3.9 μm (Figures 7d2 to 7f2). During the transport, the dust loading is also decreasing (see Figures 7a1 to 7f1), leading to lower information content for retrieving D_{eff} (see Figure 2a) and, therefore, relatively higher retrieval uncertainty (error bars in Figures 7a2 to 7f2).
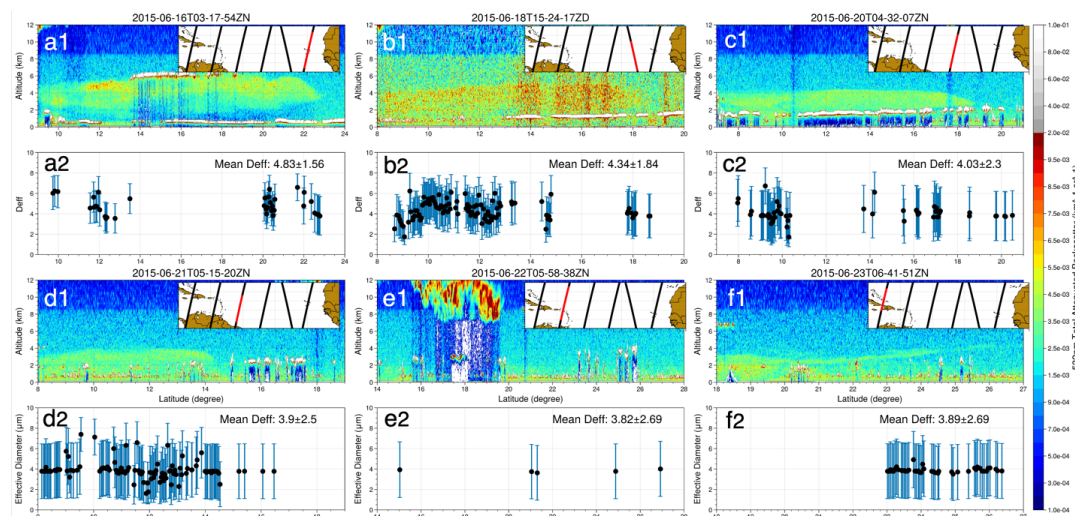
Figure 7: (a1 to f1) The CALIOP total attenuated backscatter at 532 nm on June 16th (a1), 18th (b1), 20th (c1), 21st (d1), 22nd (e1), 23rd (f1), 2013 (the orbit at upper left). (a2 to f2) The retrieved D_{eff} (black dots) of the cloud-free dust-laden profiles with the retrieval uncertainty (cyan error bars) corresponding to a1 to f1.

To prove that the MODIS-CALIOP observations snapshotted the transport processes of the same dust case that SALTRACE observes, we present the HYSPLIT back trajectories started from the MODIS-CALIOP observation on June 23rd over the Caribbean Sea, as shown in Figure 8. We set the dust layer heights at 2 km and 3.5 km at the starting point (see Figure 8b) to serve as the vertical boundaries of the observed dust plume on June 23rd (Figure 7f1). Figure

8a shows that the dust event originated from the North African source regions identified during SALTRACE (see Figure 5 in Weinzierl et al. (2016)) before June 13th. In addition, the dust case has transport trajectories overlapping with the MODIS-CALIOP observed dust plumes presented in Figure 7. Comparing Figure 8b with Figures 7a1 to 7f1, we found that the vertical height of the dust plume varies between 2 km and 6 km during transport, which agrees with

565 the vertical dust distribution observed by MODIS-CALIOP. Therefore, we conclude that the MODIS-CALIOP dust cases observe the same dust case as SALTRACE. However, we notice that the MODIS-CALIOP observational times are not perfectly consistent with the back trajectory times, implying that the retrievals presented in Figure 7 may not be the properties of the same air mass in the dust event as observed by SALTRACE. Thus, we do not expect a perfect agreement between our retrieved D_{eff} and the SALTRACE measurements.

570
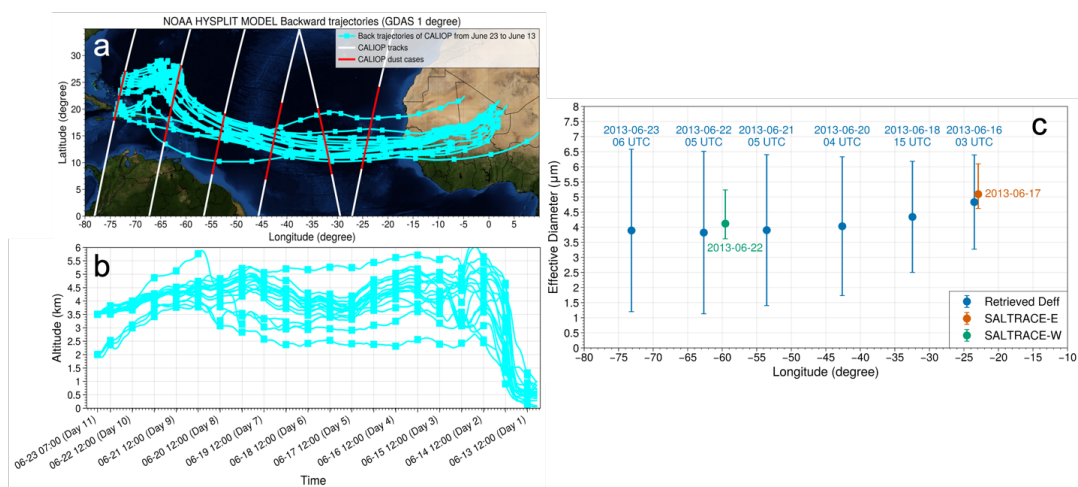
Figure 8: The distribution of the spatial (a) and the vertical (b) ensemble HYSPLIT back trajectories on the CALIOP dust case from 2013-06-23 back to 2013-06-12 (cyan rectangle solid lines). The white solid curves represent the MODIS-CALIOP orbit tracks that observed the dust cases presented in Figure 7, which are highlighted in red curves. (c) The D_{eff}
575 **versus the longitudes of the MODIS-CALIOP retrievals in Figure 7 (blue dots), the SALTRACE-E at Cape Verde (red dot) and the SALTRACE-W at Barbados (green dot). The corresponding error bars represent their retrieval uncertainties and in-situ measured uncertainties.**

Figure 8c shows the retrieved mean D_{eff} of the MODIS-CALIOP observed dust plumes in Figure 7 and the D_{eff} of
580 SALTRACE-E at Cape Verde and SALTRACE-W at Barbados. The retrieved D_{eff} on June 16th over Cape Verde (4.8 µm) is close to that of SALTRACE-E (5.1 µm). During the transport from Cape Verde (23°W) to mid-Atlantic (43°W), the D_{eff} decreases from 4.8 µm to 4.0 µm. Approaching Barbados and further the Caribbean Sea, the D_{eff} remains at 3.9 µm, which is also close to that of SALTRACE-W (4.1 µm). It validates the D_{eff} retrieval in both the short-range and long-range transport regions and demonstrates the retrieval's capability of revealing the transport process of dust
585 coarse-mode particle size in a better spatiotemporal resolution than in-situ measurements.

5 Climatological analyses

5.1 Comparison of $DAOD_{10\mu m}$ with IIR-based $DAOD_{10.6\mu m}$ and IASI-based $DAOD_{10\mu m}$

Beyond the case studies, we statistically evaluate the MODIS-CALIOP $DAOD_{10\mu m}$ by comparing it with the three independent TIR-based satellite-retrieved $DAOD_{TIR}$ datasets that are rigorously assessed through comparisons with
590   AERONET COD_{500nm}. The first one is the night-time-only IIR-based $DAOD_{10.6\mu m}$ from Z22. Note that the IIR-based retrieval has two $DAOD_{10.6\mu m}$ datasets based on two different dust PSD assumptions. We use the one based on the Fennec SAL PSD from Ryder et al. (2013a) (referred to as "Fennec-SAL $DAOD_{10.6\mu m}$") recommended from Z22. The second one is the IASI-based dataset, as mentioned in Section 1. It retrieves $DAOD_{10\mu m}$ and dust mean layer altitude based on a two-step LUT method developed by the research group at Laboratoire de Météorologie Dynamique (LMD)
595   (referred to as "IASI-LMD"). The third one retrieves $DAOD_{10\mu m}$ using IASI based on an artificial neural network (NN) method developed by the research group at Université libre de Bruxelles (ULB) (referred to as "IASI-ULB") (Clarisse et al., 2019).

As the IIR Fennec-SAL $DAOD_{10.6\mu m}$ can be easily collocated with the MODIS-CALIOP $DAOD_{10\mu m}$, we perform a
600   pixel-by-pixel comparison between the two datasets using the five-year retrievals from 2013 to 2017 at nighttime based on a two-step collocation method. As mentioned in Z22, the IIR-based retrieval is implemented on samples with the estimated $DAOD_{532nm} > 0.05$, while the MODIS-CALIOP retrieval does not carry this limitation. Consequently, we first choose the MODIS-CALIOP $DAOD_{10\mu m}$ with the corresponding estimated $DAOD_{532nm} > 0.05$ in both products. Note that the MODIS-CALIOP $DAOD_{10\mu m}$ is retrieved simultaneously with D_{eff} while the IIR Fennec-SAL
605     $DAOD_{10.6\mu m}$ was retrieved with a fixed $D_{eff} \sim 6.7$ μm. Therefore, to control the dust PSD impact on the retrieved DAOD, we further select the MODIS-CALIOP $DAOD_{10\mu m}$ with D_{eff} ranging from 4 μm to 8 μm to collocate with the Fennec $DAOD_{10.6\mu m}$.

As shown in Figure 9a, the $DAOD_{10\mu m}$ correlates with $DAOD_{10.6\mu m}$ with R = 0.7 and with $DAOD_{10.6\mu m}$ being
610   systematically lower than $DAOD_{10\mu m}$ by 25% (slope = 0.75). The difference may be attributed to the spectral difference between 10.0 μm and 10.6 μm (see Figure 5c), which ranges from 0.5 to 0.8 for D_{eff} ranging from 4 μm to 8 μm. In addition to spectral differences, several factors may have caused the variability of the collocated pixels between the two datasets. Firstly, although the collocated $DAOD_{10\mu m}$ are pre-selected based on D_{eff}. The impact of dust PSD on the retrieved DAOD still exists, as it is challenging to find enough pixels with the same D_{eff} as the Fennec SAL
615   observation. Secondly, the treatments of RI in the two studies are also different. In Z22 a relatively simple method is used to assign the Di-Biagio RI to different regions while we utilize the DustCOMM-2021 to help assign Di-Biagio RI in this study (see Appendix C). Furthermore, the MODIS-CALIOP retrieval has evolved from the IIR-based retrieval from Z22 with three improvements, namely the lower detector noise from MODIS, the improved retrieval methods, and the enhanced dust RI assumptions. These differences may have also directly affected the pixel-by-pixel
620   comparison.

Thanks to the abovementioned improvements, in Figure 9b, the histogram of the absolute DAOD uncertainty of $DAOD_{10\mu m}$ is reduced by ~55% from 0.2 to 0.09 in terms of the mean value compared with that of $DAOD_{10.6\mu m}$. In Figure 9c, the relative uncertainty of $DAOD_{10\mu m}$ is substantially reduced compared with that of $DAOD_{10.6\mu m}$, especially

625   for retrievals with small DAOD value (e.g., $DAOD_{10\mu m} < 0.1$). Consequently, we conclude that the MODIS-CALIOP $DAOD_{10\mu m}$ is generally consistent with the IIR-based $DAOD_{10.6\mu m}$ from Z22 with a substantial improvement regarding the retrieval uncertainty
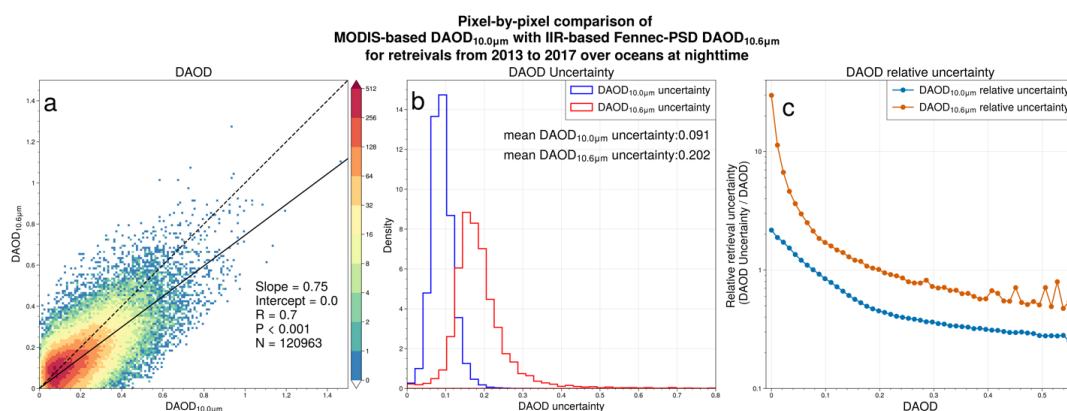
630

Figure 9: The pixel-by-pixel comparison of MODIS-CALIOP $DAOD_{10\mu m}$ with the IIR-based Fennec-SAL $DAOD_{10.6\mu m}$ from Z22 for retrievals from 2013 to 2017 over oceans at nighttime. (a) The joint histogram of $DAOD_{10\mu m}$ and $DAOD_{10.6\mu m}$. The solid black line is the linear regression of the two datasets. The R, P and N at the lower right represent the Pearson correlation coefficient, p-value and the number of pixels of the linear regression. (b) The probability density

635   **function (PDF) of $DAOD_{10\mu m}$ uncertainty (blue) and $DAOD_{10.6\mu m}$ uncertainty (red). (c) The mean relative retrieval uncertainty (i.e., DAOD uncertainty / DAOD) of $DAOD_{10\mu m}$ (blue) and $DAOD_{10.6\mu m}$ (red). The y-axis is on a logarithmic scale.**

Unlike the comparison with the IIR-based retrieval, the orbit difference between the MODIS-CALIOP and IASI

640   observations and the cloud-free dust sampling difference between the corresponding retrievals prevent the pixel-by-pixel comparison with the Level-2 data (Zheng et al., 2022). Therefore, we alternatively perform the climatological comparison among the aggregated 5° longitude by 2° latitude Level-3 seasonal mean MODIS-CALIOP, IASI-LMD and IASI-ULB $DAOD_{10\mu m}$ based on five-year data from 2013 to 2017 in both daytime and nighttime. The 5° by 2° seasonal mean IASI-LMD and IASI-ULB $DAOD_{10\mu m}$ are aggregated from the corresponding 1° by 1° monthly mean

645   Level-3 products. Note that both seasonal mean IASI DAODs are divided by the total number of AOD samples. To be consistent, in our retrieval, the seasonal mean $DAOD_{10\mu m}$ is averaged by the total number of cloud-free aerosol samples ($N_{aerosol}$ in Figure S9). Similar to Z22, we highlight three dust-transport regions, North Atlantic (NA), Indian Ocean (IO) and North Pacific (NP) as shown in Figure 10.
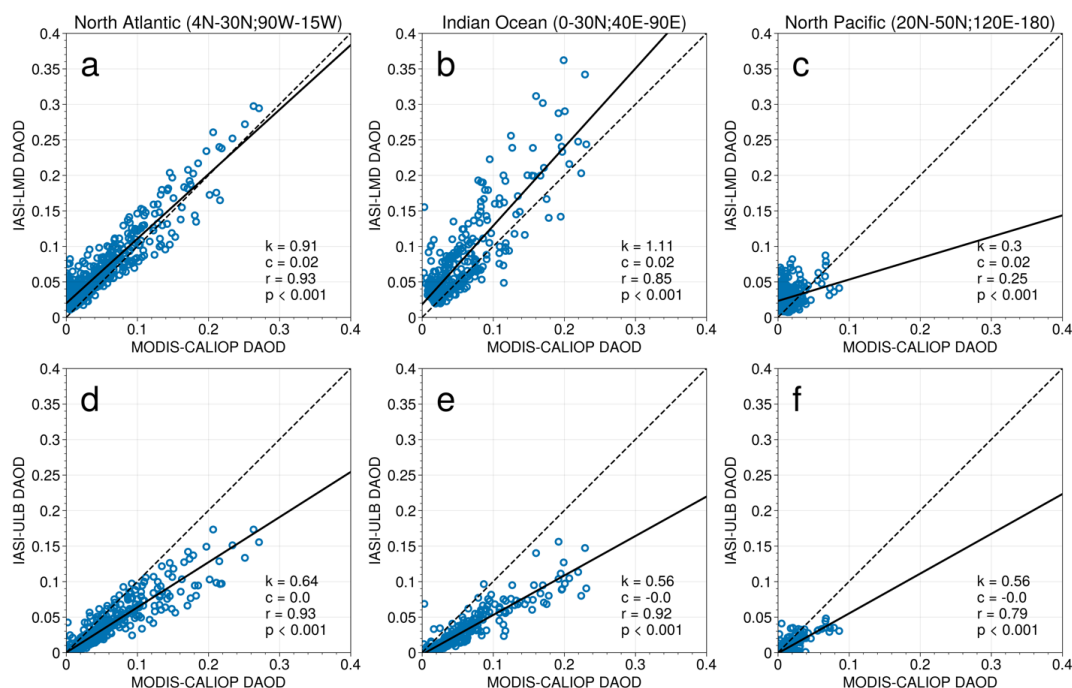
Figure 10: The comparisons of the seasonal mean MODIS-CALIOP DAOD$_{10\mu m}$ versus IASI-LMD (a,b,c) and IASI-ULB (d,e,f) DAOD$_{10\mu m}$ over NA (a,d), IO (b,e) and NP (c,f) from 2013 to 2017. Each point in the scatterplots represents a seasonal mean DAOD$_{10\mu m}$ in one of the 5° by 2° grids for a specific year from 2013 to 2015. The solid black lines are the linear regressions of each comparison, while the black dash lines are the reference one-to-one lines. The k, c, r and p at the upper right of each panel represent each linear regression's slope, intercept, correlation coefficient and p-value.

Figure 10 shows the comparisons of 5° by 2° gridded seasonal mean MODIS-CALIOP DAOD$_{10\mu m}$ with the two IASI DAOD$_{10\mu m}$ over the three dust-transport regions from 2013 to 2017. MODIS-CALIOP DAOD$_{10\mu m}$ over NA and IO are highly correlated and consistent with IASI-LMD DAOD$_{10\mu m}$ with R = 0.9,0.8 and k = 0.9,1.1, respectively, as shown in Figures 10a and 10b. However, for optically thin dust (e.g., DAOD < 0.1), IASI-LMD DAOD$_{10\mu m}$ is systematically ~0.02 greater than MODIS-CALIOP DAOD$_{10\mu m}$ as shown from the intercepts of the linear regression in Figures 10a and 10b. In addition, the two datasets have poor agreement over NP (R = 0.2). In contrast, MODIS-CALIOP DAOD$_{10\mu m}$ achieves a better correlation over the dust-transport regions (including NP) than the comparison with IASI-LMD DAOD$_{10\mu m}$ (see Figures 10d-10f). It is mainly because both retrievals mostly avoid contamination from sub-pixel clouds and background aerosols, which should be the reason for the high bias of the IASI-LMD optically thin dust (DAOD$_{10\mu m}$ < 0.1) DAOD$_{10\mu m}$. However, IASI-ULB DAOD$_{10\mu m}$ is 40%-60% lower than that of MODIS-CALIOP and IASI-LMD DAOD$_{10\mu m}$ over the three dust-transport regions (k = 0.6,0.5,0.4 in Figures 10d-10f).

24

670   Although the discrepancy of the two IASI-based $DAOD_{10\mu m}$ is non-negligible, the two datasets achieve good agreements with AERONET because the different assumptions of TIR-to-VIS DAOD ratios offset the $DAOD_{10\mu m}$ difference. As they assumed similar dust RIs (e.g., OPAC RIs) and spherical dust, the disagreement of the $DAOD_{10\mu m}$ could be due to the different *a priori* dust PSDs. IASI-ULB assumes a monomodal dust PSD with a geometric mean radius at 0.5 μm (i.e., mean diameter at 1.0 μm). It is much smaller than the IASI-LMD assumed coarse-mode dust PSD with an effective radius at 2.3 μm (i.e., effective diameter = 4.6 μm), possibly leading to the systematically lower

675    $DAOD_{10\mu m}$ compared with MODIS-CALIOP and IASI-LMD $DAOD_{10\mu m}$. Because MODIS-CALIOP D_{eff} has a climatological value ranging from 4.0 to 5.0 (see Figure 11, detail in Section 5.2), which is closer to 4.6 μm, MODIS-CALIOP $DAOD_{10\mu m}$ shows better consistent with the IASI-LMD $DAOD_{10\mu m}$. This non-negligible dependency of the retrieved $DAOD_{10\mu m}$ to dust PSD is also presented in Z22. It highlights the importance of the spatiotemporal variation of dust PSD and the advantage of the observational constraint on both $DAOD_{10\mu m}$ and dust coarse-mode PSD from

680   the MODIS-CALIOP retrieval.

5.2 Spatiotemporal variation of dust D_{eff}

One of the main objectives of this study is to provide a climatological view of dust coarse-mode size variation during transport in a global coverage from satellite observations, which has not yet been available in the literature, as far as

685   we know, due to the difficulties mentioned in Section 1. In this section, we present the spatiotemporal variation of D_{eff} in terms of seasonal variation, the regional difference among dust-transport regions and longitudinal-mean variation within dust-transport regions based on the five-year retrieval data from 2013 to 2017.

Different with seasonal mean $DAOD_{10\mu m}$, the denominator of the seasonal mean D_{eff} is the number of samples with successful retrievals only. Noting that the retrieval uncertainty is large for optically thin dust (i.e., $DAOD_{10\mu m} < 0.1$,

690   see Figure 9c), we consider that the seasonal mean $DAOD_{10\mu m} < 0.005$ is mainly contributed by optically thin dust and therefore mask the seasonal mean D_{eff} with seasonal mean $DAOD_{10\mu m} < 0.005$ to focus on more confident D_{eff} retrievals. We found that the seasonal variation of D_{eff} is highly correlated with that of $DAOD_{10\mu m}$. For example, the largest D_{eff} over NA and IO occurs in summer, while the peak of D_{eff} over NP happens in spring. As dust extinction in TIR is more sensitive to coarse-mode dust (Ryder et al., 2019), it is reasonable to find that the greater the $DAOD_{10\mu m}$,
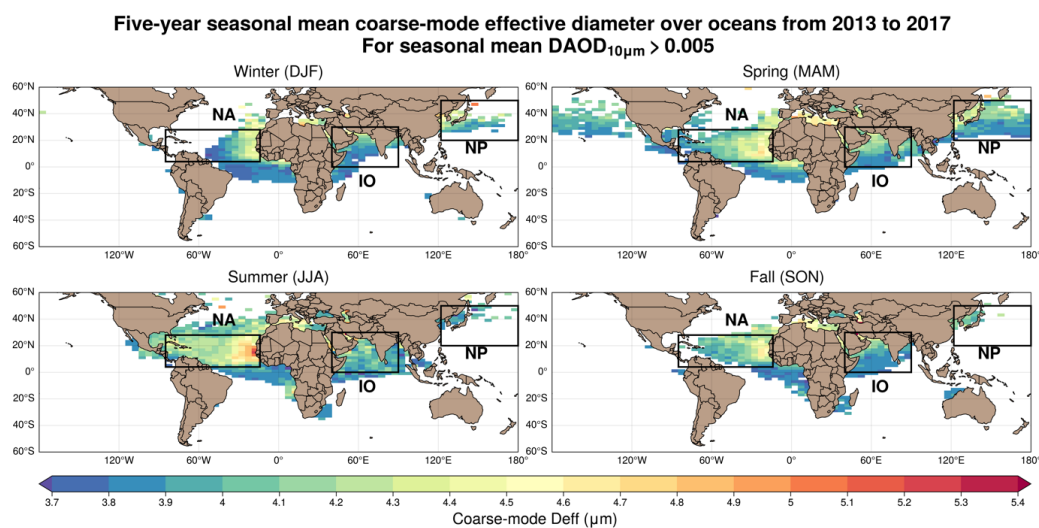
695   the coarser dust is in the atmosphere.

Figure 11: 2013-2017 five-year averaged seasonal mean D_{eff} masked by the five-year seasonal mean $DAOD_{10\mu m} > 0.005$ in winter (a), spring (b), summer (c) and fall (d). The black boxes indicate the three defined dust-transport regions as same as in Figure 9.

700

In terms of regional differences, we found that the maximal seasonal D_{eff} over IO (~4.2 μm in summer, Figure 11c) and NP (~4.2 μm in spring, Figure 11b) are ~22% lower than that over NA (~5.4 μm in summer, Figure 11c). It suggests that the coarse-mode dust is frequently found over NA but not over IO and NP. It is expected over NP because

705   the transport distance from source regions located in East Asia to NP is much longer than that from North Africa to NA (Alizadeh-Choobari et al., 2014). In addition, the emitted and transported dust PSD from Asia is possible to be finer than that from North Africa and Arabia due to the radiative feedback on dust emission (Woodage and Woodward, 2014). As a result, there is less chance for coarse dust particles to survive till over NP. In contrast, although dust from the Middle East to IO has a similar transport distance as that over NA, fewer coarse dust particles are found over IO.

710   As the retrieval samples are distributed similarly over the three transport regions for all seasons as shown in Figure S9, it is less likely to have sampling bias between regions. One of the possible reasons that the long-range transport dust from the Middle East is not within elevated mixed layers (Carlson, 2016), such as SAL over NA, that triggers static instability and strong vertical turbulence to sustain coarse dust particles for a longer lifetime (Gutleben and Groß, 2021; Gasteiger et al., 2017). However, due to insufficient in-situ measurements on dust PSD in the Middle East

715   (Adebiyi et al., 2020b), what causes the regional differences in dust particle size after long-range transport remains open and needs further investigation in the future.
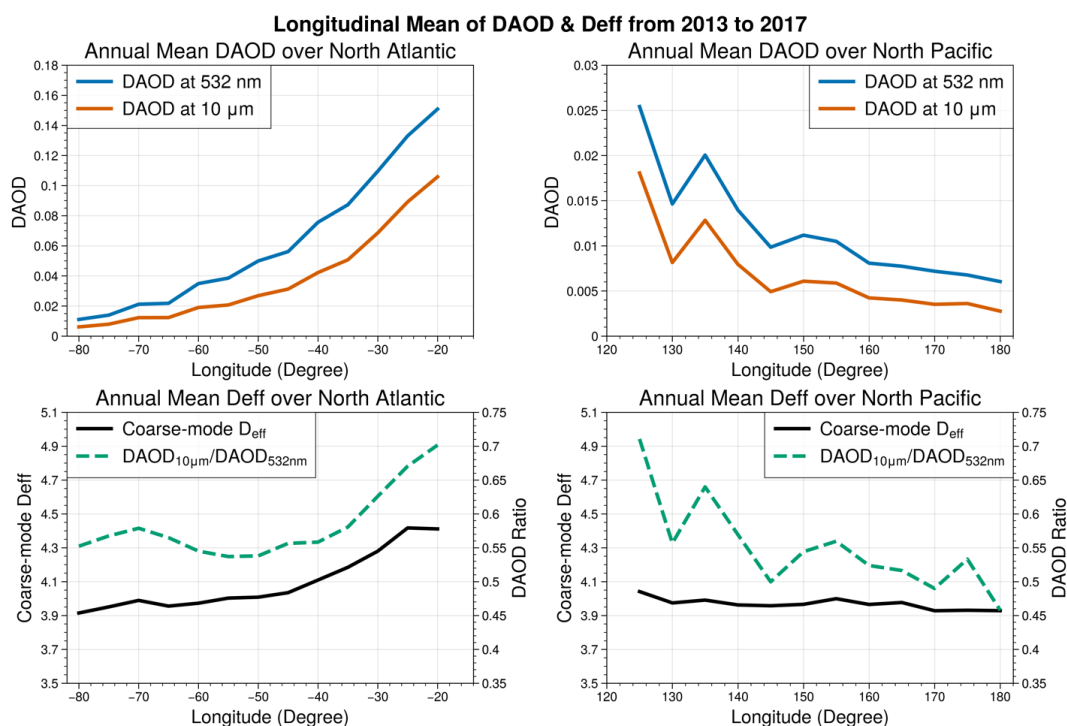
Figure 12: The annual longitudinal mean DAOD$_{10\mu m}$ (blue curves), DAOD$_{532nm}$ (red curves), the DAOD ratio of DAOD$_{10\mu m}$ to DAOD$_{532nm}$ (green dash curves) and D$_{eff}$ (black curves) over the North Atlantic (a,c) and the North Pacific (b,d).

As mentioned in Section 5.1, the assumed dust PSD impacts heavily on both the retrieved DAOD$_{10\mu m}$ and the theoretical TIR-to-VIS DAOD ratio. Because our retrieval provides simultaneous DAOD$_{10\mu m}$ and D$_{eff}$ and the synergetic CALIOP estimated DAOD$_{532nm}$, we further investigate the relationship between D$_{eff}$ and the observational-based TIR-to-VIS DAOD ratio (defined as DAOD$_{10\mu m}$/DAOD$_{532nm}$). From the view of longitudinal transport for Saharan dust and Asian dust, we demonstrate the annual longitudinal mean DAOD$_{532nm}$ and DAOD$_{10\mu m}$ over NA and NP (Figures 12a and 12b). They both show a consistent variation between DAOD$_{532nm}$ and DAOD$_{10\mu m}$ with a decreasing trend westward over NA and eastward over NP, convincing the reliability of the DAOD$_{10\mu m}$ retrievals described in Section 5.1. Figures 12c show that the corresponding DAOD ratio over NA decreases by 23% westward from 18°W to 40°W and 8% from 40°W to 80°W. As coarse-mode particles dominate the dust extinction in TIR, the reduction of the DAOD ratio reflects the faster decrease of DAOD$_{10\mu m}$ and, thus, implies a loss of coarse-mode dust loading in the column, which also can be inferred by the decreasing of D$_{eff}$. In Figure 12c, we found that the decreasing trends of D$_{eff}$ and DAOD ratio are highly correlated. It demonstrates a ~20% reduction of DAOD ratio and a ~7% decrease of mean D$_{eff}$ during the transport to the mid-Atlantic, while there are less than 10% and 2% decrease of DAOD ratio and mean D$_{eff}$ during the rest of the NA transport. The transport pattern over NA is also similar with the dust case observed by SALTRACE presented in Section 4.2.2. However, in Figure 12d, we found a rapid fluctuation of the DAOD ratio due to the fewer retrieval samples (Figure S9) and higher retrieval uncertainty from 120°E to

140°E, which is 'gainst D_{eff}'s relatively stable decreasing rate. Despite that, we found a less than 10% reduction of D_{eff} throughout the eastward transport to 180°, suggesting a stable trend of dust coarse-mode size during the NP transport.

740

Note that dust particle size varies in the day-to-day transports, which is not visible in the long-term averaged longitudinal transport. To provide details on the variation of D_{eff} in different size ranges during transport over NA and NP in their peak season, we present the population distribution of D_{eff} longitudinally in summer over NA and spring over NP. We first slice the NA region from 4°N to 30°N into seven sub-regions at 10° longitude intervals, as shown

745   in Figure 13h. Within each sub-region box, we present the histogram and the cumulative distribution function (CDF) of D_{eff} of all the optically thick dust (i.e., $DAOD_{10\mu m} > 0.1$) in the summer from 2013 to 2017. To better visualize the variation of D_{eff} during the transport, within each sub-region box, the histogram and CDF (blue curves in Figures 13a to 13g) are compared with those from the previous (i.e., eastward) box are also presented (red curves in Figures 13b to 13g).
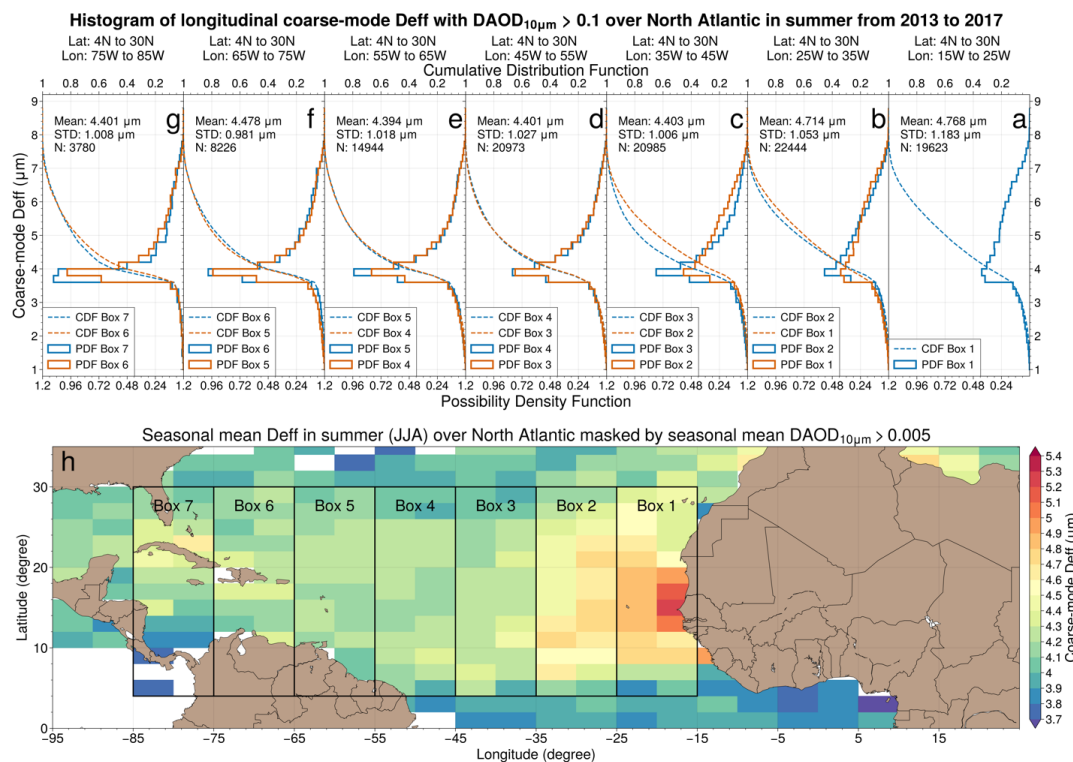
Figure 13: The histogram (solid curves with the bottom x-axis) and the cumulative distribution function (dash curves with the top x-axis) of D_{eff} with $DAOD_{10\mu m} > 0.1$ within each longitudinal box from west to east ranging from 1 (a) to 7 (g) over the NA in the summer from 2013 to 2017. Blue curves represent D_{eff} samples within the current box. Orange curves represent D_{eff} samples within the previous box eastward. (h) The geolocation boundaries of each longitudinal box on top of

755   **the seasonal mean D_{eff} were masked by seasonal mean $DAOD_{10\mu m} > 0.005$ over the NA in the summer from 2013 to 2017.**

Figures 13a to 13b show a slightly decrease of the population of D_{eff} greater than 5.5 μm. From Figures 13b to 13c, according to the CDFs, the contribution of $D_{eff} > 5$ μm to the total number reduced from 40% to 20%. In PDFs, there is a ~50% reduction in the population of $D_{eff} > 5$ μm, while ~20% more dust with $D_{eff} \sim 4$ μm is found, leading to the reduced mean D_{eff} from 4.7 μm to 4.4 μm. Meanwhile, the peak of the PDFs in Figures 13a to 13g remains stable at 4.0 μm, while the number of samples decreases gradually, as shown in PDFs in Figures 13d to 13g, indicating that less coarse-mode dust can be transported to Boxes 5 to 7 (55°W to 85°W).

The result suggests that ~50% of relatively coarser dust ($D_{eff} > 5$ μm) tends to drop out when transported to the mid-Atlantic (25°W to 35°W), which is ~2000 km away from source regions over North Africa. Afterward, from the mid-Atlantic to the Caribbean Sea, the mean D_{eff} remains almost unchanged, agreeing with the arguments from previous studies that the stabilization of coarse-mode dust PSD during the long-range transport (Weinzierl et al., 2017; Denjean et al., 2016; Ryder et al., 2019). Additionally, dust samples with $D_{eff} > 5$ μm can still be found even at 65°W and 75°W (see Figures 13f and 13g) but with a relatively lower frequency (~20%). In other words, super-coarse dust particles, although rare, are still possible to be carried on a long-distance journey during the transport over NA (Van Der Does et al., 2018), which act against the gravitational settling theory by Stoke's law (Ginoux, 2003; Bagnold, 1974).
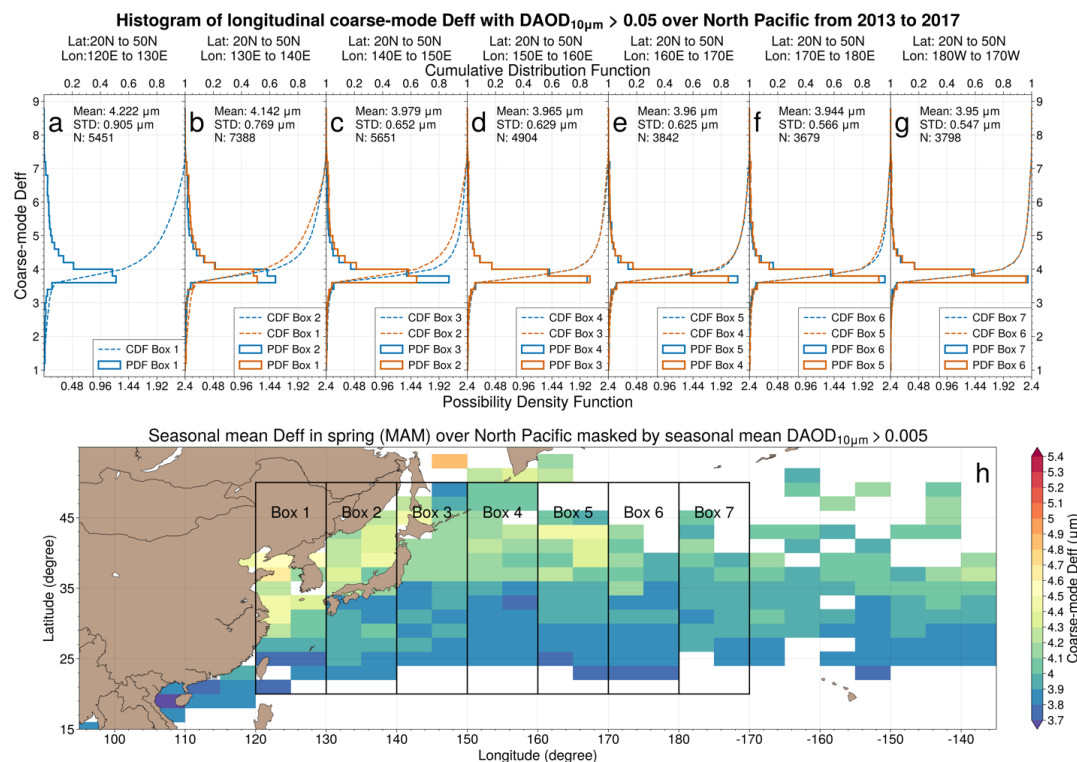

Figure 14: Same as Figure 13 but for D_{eff} with $DAOD_{10\mu m} > 0.1$ within each longitudinal box from west to east ranging from 1 (a) to 7 (g) over the NP in the spring from 2013 to 2017.

Unlike the Trans-Atlantic dust, Asian dust transport over NP experiences longer travel distances from the East Asian source regions and therefore has systematically smaller particle size. With the same method as Figure 13, we present the histograms of D_{eff} with $DAOD_{10\mu m} > 0.05$ (according to the lower seasonal mean $DAOD_{10\mu m}$ over NP) within seven longitudinal boxes, as shown in Figure 14. During the transport, the mostly unchanged PDFs with $D_{eff} > 4$ μm from

780 Box 1 (130°E) to Box 2 (140°E) only reduced ~10% from Box 2 to Box 3 (150°E). The CDFs are stable throughout the transport from Box 3 to Box 7 regardless of the total number of dust samples decrease. Compared with dust over NA, only ~5% of dust with $D_{eff} > 5$ μm can be found after transporting to Box 3. The relatively homogenous and stable distribution of $D_{eff} \sim 4$ μm suggests that the coarse-mode dust particles over NP may also have longer lifetimes than expected by the stand-alone gravitational settling theory. However, as $DAOD_{10\mu m}$ and the number of successful

785 retrievals over NP are lower than that over NA and IO, the relatively higher retrieval uncertainty prevents us from drawing a clear conclusion. Future studies are recommended to validate the satellite retrieved D_{eff} by in-situ measured Asian dust PSDs.

6 Discussions and Conclusions

790 This study developed a novel retrieval algorithm for $DAOD_{10\mu m}$ and the coarse-mode dust PSD represented by D_{eff} using the collocated CALIOP and MODIS observations. The D_{eff} retrieval is detailly validated through three case studies in Aug 2015, Jan 2008 and June 2013, respectively.

We validate the $DAOD_{532nm}$ matching with the AERONET total AOD at Cape Verde in the 2015 case study. Despite

795 the spectral difference preventing the "apple-to-apple" comparison of $DAOD_{10\mu m}$ with AERONET, the relatively good correlation between $DAOD_{10\mu m}$ and the AERONET-validated $DAOD_{532nm}$ demonstrate the $DAOD_{10\mu m}$ retrieval's reliability. Afterward, we present the consistency of the monomodal PSDs corresponding to the retrieved D_{eff} with the AER-D PSD and SAMUM-2 PSD as well as their TIR optical properties in the 2015 and 2008 cases. The 2013 case validates the D_{eff} retrieval in both the short-range (Cape Verde) and long-range (the Caribbean Sea) transport regions

800 by comparing with SALTRACE dust PSD and demonstrates the retrieval's capability of revealing the transport process of dust coarse-mode particle size in a better spatiotemporal resolution than in-situ measurements. The results convince us that the $DAOD_{10\mu m}$ and D_{eff} retrieval dataset can provide a better constraint on regional and global LW DRE uncertainties due to DAOD and dust PSD. However, an assumption of dust RI is still needed.

805 We apply the retrieval to five-year MODIS-CALIOP data from 2013 to 2017 and compare the DAOD retrieval with IIR-based and IASI-based retrieval. As an improved version compared with the IIR-based retrieval, the MODIS-CALIOP retrieval reduced ~50% of DAOD uncertainty and achieves good consistency (R = 0.7 in Figure 9). In the climatological comparison with the seasonal mean IASI-based $DAOD_{10\mu m}$, MODIS-CALIOP $DAOD_{10\mu m}$ reaches a better agreement with IASI-LMD $DAOD_{10\mu m}$ over NA (R = 0.9) and IO (R = 0.8) than that over NP (R = 0.2).

810 Meanwhile, the IASI-ULB $DAOD_{10\mu m}$ over the three regions are highly correlated with MODIS-CALIOP $DAOD_{10\mu m}$, while they are systematically underestimated possibly due to the D_{eff} of the pre-assumed dust PSD is significantly

lower than that of IASI-LMD $DAOD_{10\mu m}$ and the climatological D_{eff}. The discrepancy of the two AERONET-evaluated IASI $DAOD_{10\mu m}$ datasets reveals that the dependency of TIR-to-VIS DAOD ratios and the retrieved $DAOD_{10\mu m}$ to dust PSD is non-negligible, which is also proved in Z22. It highlights the importance of considering the spatiotemporal variation of dust D_{eff} in TIR retrievals.

A global and climatological analysis of the five-year D_{eff} retrievals from -60°N to 60°N over oceans is presented. Comparing D_{eff} among the three transport regions, we found that seasonal mean D_{eff} over IO (3.9-4.2 μm) is up to ~22% lower than that over NA (4.1-5.4 μm) depending on different seasons, implying a shorter lifetime of coarse-mode dust particles transported from the Middle East to IO than that from North Africa to NA. For D_{eff} variation during transport, over NA, we found a ~50% reduction of retrievals with D_{eff} > 5 μm from 15°W to 40°W and a relatively stable D_{eff} at ~ 4 μm throughout the Caribbean Sea. The D_{eff} result from 15°W to 40°W differs from the IASI-retrieved effective radius distribution over NA in Peyridieu et al. (2013), which presented an almost constant value at 2 μm during summer throughout the transport. In addition, the prevailing dust with D_{eff} at ~ 4 μm and a small portion of dust with D_{eff} > 5 μm (5%-20%) found after long-term transport in both NA and NP can hardly be explained by the stand-alone gravity settling theory. The results provide observation-based transport patterns of the coarse mode dust size over oceans, which can be used to evaluate the simulated dust coarse mode PSD in dust transport models.

However, there are serval limitations for our retrieval. First of all, the case-study validation of D_{eff} is limited to three field campaigns. Extended comparisons with other in-situ measurements, especially over Mediterranean, IO and NP, should be realized further to validate the applicability and significance of the proposed approach. Secondly, our retrieval is still not applicable for observations over land due to the uncertainties from land surface temperature and emissivity. Nonetheless, with more reliable databases of land surface characteristics, this portable retrieval algorithm can be easily extended to cover the dust source regions. Thirdly, the limited spatial coverage of CALIOP restrains the application of our data to regional studies. Extending the retrieval to off-CALIOP-track MODIS pixels is recommended for future studies.

Appendix A: The cloud-free clean radiative closure benchmark between the CRTM-DISORT calculated and
840   **the MODIS-observed BTs**

In this study, the uncertainties contributed by the auxiliary data, the radiative transfer simulation, and the observational errors is evaluated through the radiative closure benchmark between the CRTM-DISORT calculated and the MODIS-observed BTs under cloud-free and clean (without dust) conditions based on the collocated MODIS and CALIOP data from 2007 to 2010.

845

Figures A1a and A1c show the BT discrepancies (referred to as "dBT") between the simulations and the observations for daytime and nighttime cloud-free and clean cases over oceans at three MODIS TIR bands. Figures A1b and A1d show the corresponding discrepancies of the cloud-free spectral BT differences (BTD) between 11 μm and 12 μm (blue curve, referred to as "$dBTD_{11-12}$") and that between 8.5 μm and 12 μm (red curve, referred to as "$dBTD_{08-12}$").

850   Both dBTs and dBTDs are unbiased (i.e., with a peak and a mean value centered at zero) in both daytime and nighttime, demonstrating a remarkable consistency between the CRTM-DISORT simulation and the MODIS observation. For the three single TIR BTs, because the 8.5-μm and 11-μm bands are the cleaner (i.e., less water vapor absorption) than the 12-μm band that is the most water-vapor-absorptive, the standard deviations of dBT at 8.5 μm and 11 μm are lower (0.78 – 0.86 K) than that at 12 μm (0.88 – 0.9 K). Interestingly, the errors of the two dBTDs are substantially reduced

855   to the range of 0.2 to 0.4 K as the errors from the assumed atmospheric states at each band are canceled out, especially the $dBTD_{11-12}$ (0.18 K at nighttime and 0.21 K at daytime), which is sensitive to DAOD as explained in section 3.2. The smaller uncertainties in dBTDs are probably due to error cancellations. For example, if AMSR-E underestimates the SST, the simulated BT would be colder than the observation because of the overestimated surface-emitted radiance. However, the underestimation happens in all three TIR bands, and the error cancels each other to some

860   extent, leading to smaller uncertainty in dBTDs.

Overall, one standard deviation of dBTs and dBTDs represents the retrieval uncertainty due to the atmospheric auxiliary data, the radiative transfer simulation, and the observational errors, which is revisited in section 3.2.
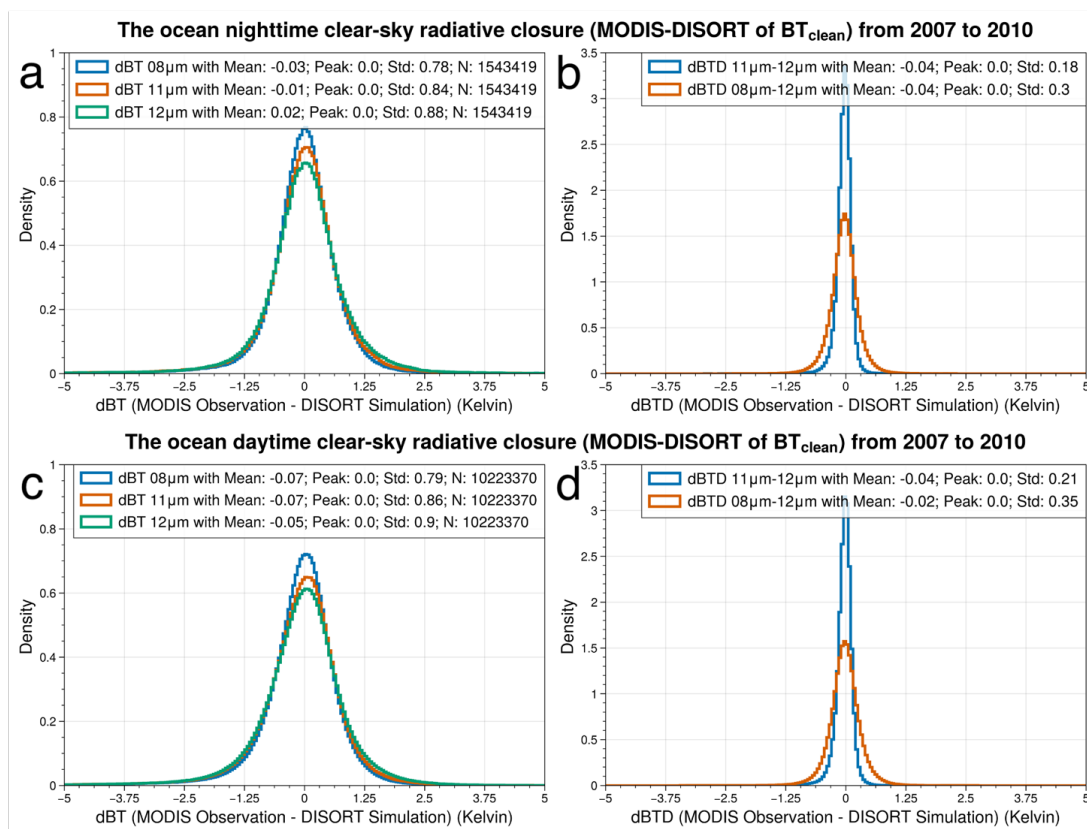
Figure A1: The nighttime (a) and daytime (c) cloud-free and clean sky dBTs at the MODIS 8.5-μm (blue), 11-μm (orange) and 12-μm (green) bands. The nighttime (b) and daytime (d) cloud-free clean sky dBTD$_{8-12}$ (orange) and dBTD$_{11-12}$ (blue).

Appendix B: Pre-processing of the cloud-free dust detection from the collocated MODIS and CALIOP observation

The first step of the retrieval is to identify high-quality cloud-free dust-laden observations. Due to the different spatial coverage of MODIS and CALIOP, the retrieval requires collocated data from both sensors, which is done in the following steps. First, we refer to the MODIS-AUX product (Partain, 2007) developed for CloudSat to find along-CloudSat-track MODIS pixels for two reasons. First, each along-CloudSat-track profile has 15 collocated MODIS pixels in the MODIS-AUX product. Each MODIS pixel contains the MODIS Level-1B radiances and Level-2 geometries. Using the 15 collocated MODIS pixels saves computational time from accessing the original terabyte-scale Level-1B products (Zheng et al., 2021). Second, the along-track orbits of CALIPSO and CloudSat are highly synchronized. It allows each along-CALIPSO-track profile to quickly match the nearest pixel among the 15 collocated along-CloudSat-track MODIS pixels. However, noting that the MODIS viewing zenith angle of the collocated pixels are not exactly nedir as CALIOP has, which is also considered in our retrieval (See Table 1).

33

880

The CALIOP "LID_L2_05kmAPro-Standard-V4" product has a 5 km along-track resolution, while the MODIS-AUX product is 1 km. To address this spatial difference, we reference the 1-km along-CALIOP-track geolocation records from the "IIR_L2_Track-Standard-V4" product, which provides five records with 1-km resolution in each 5-km CALIOP profile. Each of the five 1-km geolocation records is then used to find the nearest along-CloudSat-track

885 MODIS pixels. The corresponding MODIS Level-1B 1-km TIR BTs, BT uncertainties and the MODIS sensor's geometries (i.e., viewing/solar zenith/azimuth angles) are then assigned to each geolocation record.

Similar to the cloud masking process as in Z22, we use the collocated 1-km "Was_Cleared_Flag_1km" originated from the "IIR_L2_Track-Standard-V4" product to screen out MODIS pixels containing sub-pixel clouds that are

890 detected by the single-laser-shot in 333 m along-track footprint. Finally, the remained cloud-free 1-km MODIS pixels within each 5-km CALIOP profile are averaged, forming the 5-km collocated MODIS-CALIOP cloud-free product.

After cloud masking, dust detection also follows the procedures described in Z22. Firstly, we identify the high-quality CALIOP backscatter profiles by applying the extinction control flag ("Extinction_QC_Flag_532 = 0, 1, 16, 18"

895 (Winker et al., 2013; Yu et al., 2015a)) to the 5-km MODIS-CALIOP cloud-free product. Next, we apply the cloud-aerosol discrimination (CAD) score to select the profiles containing all detected features with CAD between -100 to -90 to ensure the quality of the detected aerosol layers (Yu et al., 2019). Finally, the selected CALIOP backscatter profiles are further used to distinguish dust from non-dust aerosols. The separation is based on the contrast of the DPR between dust and non-dust aerosols. The higher the non-sphericity and particle size, such as dust, the lower the DPR.

900 Therefore, the DPR of dust aerosols (δ_d) is usually higher than that of other non-dust aerosols (δ_{nd}). Accordingly, a vertically resolved fraction $f_d(z)$ of dust backscatter ($\beta_d(z)$) to the observed backscatter ($\beta(z)$) (i.e., $f_d(z) = \beta_d(z)/\beta(z)$), is estimated by the observed particulate DPR $\delta(z)$, δ_d and δ_{nd} as

$$f_d(z) = \frac{(\delta(z) - \delta_{nd})(1 + \delta_d)}{(1 + \delta(z))(\delta_d - \delta_{nd})} \qquad (B1)$$

Following Yu et al. (2015a) and Z22, the lower and upper limits of δ_{nd} are set to 0.02 and 0.07 and δ_d to 0.20 and

905 0.30, respectively. The final $f_d(z)$ is set to the mean value of the upper bounds ($\delta_d = 0.3$ and $\delta_{nd} = 0.07$) and lower bounds ($\delta_d = 0.2$ and $\delta_{nd} = 0.02$). Due to the observed particulate DPR uncertainty, the value of $f_d(z)$ can exceed 1 or below 0, which are set to be 1 and 0, respectively. Finally, we obtain the backscatter profile of dust aerosol as

$$\beta_d(z) = f_d(z) \cdot \beta(z) \qquad (B2)$$

which serves as the dust vertical distribution to scale the input DAOD in the CRTM-DISORT simulation. Note that

910 the extinction coefficient profile can be obtained by multiplying $\beta_d(z)$ with an *a priori* dust extinction-to-backscatter ratios (i.e., Lidar ratios (LR)) for dust aerosol. According to previous studies for the dust LR (Haarig et al., 2022; Liu et al., 2002; Liu et al., 2008; Kim et al., 2020), we further calculate the column integrated DAOD at 532 nm (referred to as "DAOD$_{532nm}$") by assuming a dust LR at 44 sr with ± 10 sr uncertainty. However, the DAOD$_{532nm}$ uncertainty contributed by LR is beyond this study and will not be discussed. Readers are referred to Kim et al. (2020) for details.
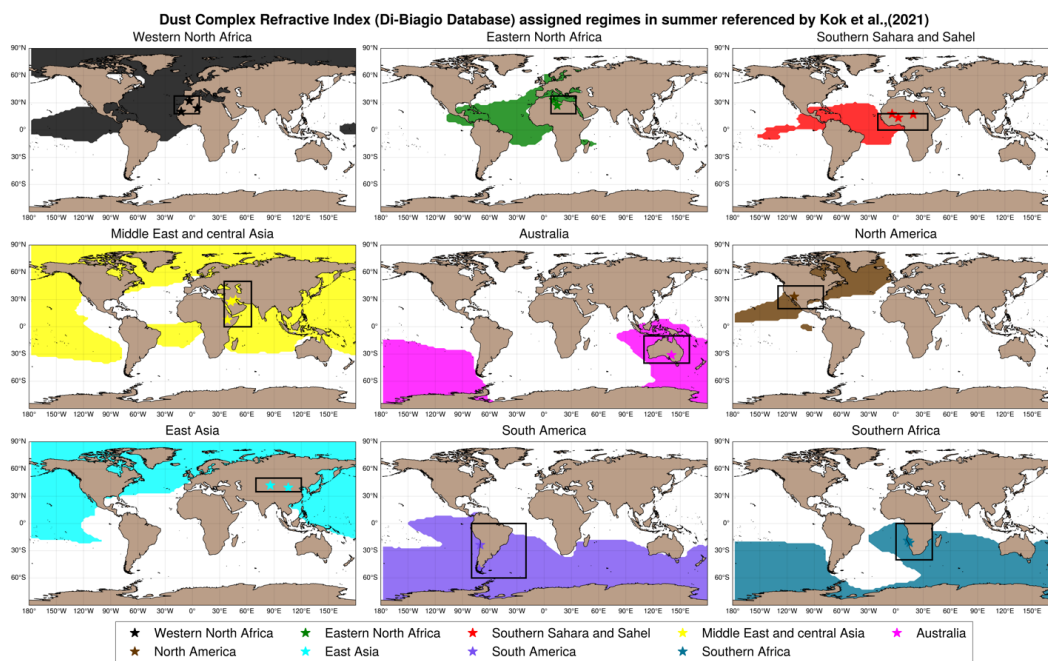
915

However, the DPR-based method is likely to include the contribution of sea salt over open oceans and generate non-zero $DAOD_{532nm}$ even without dust, especially in daytime when CALIOP has lower quality due to the solar contamination. The possible reason is that sea salt would have DPR close to dust when their relative humidity is low (e.g., < 50%) (Haarig et al., 2017). Therefore, after deriving $DAOD_{532nm}$, we further use the CALIOP VFM (i.e., the

920 "Atmospheric_Volume_Description" in the "LID_L2_05kmAPro-Standard-V4" product; see Section 2.1 and Table 1) to filter the profiles that has no dust, or polluted dust or marine dust layers. Finally, the rest of profiles are considered as cloud-free dust profiles for retrievals.

Appendix C: Assignments of dust long-wave refractive index

925 Note that assigning dust RIs from different source regions to the observed dust aerosol over the ocean should follow the dust global transport patterns. Accordingly, we applied the fractional contribution over oceans supplied by various dust source regions from the DustCOMM-2021 dataset developed by Kok et al. (2021a). This dataset provides the seasonally resolved global distribution of the fractional contribution of DAOD from nine defined dust source regions (see Figure C1) by integrating observational constraints on dust properties and abundance into an ensemble of GCM

930 simulations, gridded with a resolution of 2.5° longitude by 1.9° latitude. In other words, for each grid cell in each season, there are nine fractions representing the contributions from nine source regions, indicating the probability of where the DAOD that occurs in a grid cell in a particular season originated. We use this data set to choose the appropriate *a priori* dust RIs from different source regions for our retrieval over oceans.

Dust Complex Refractive Index (Di-Biagio Database) assigned regimes in summer referenced by Kok et al.,(2021)

35

935 **Figure C1: The assignment of the source region-resolved dust refractive indices from Di Biagio et al. (2017) is based on which of the nine main source regions provided a fractional contribution to SW DAOD that exceeds 0.1, which is shown here for summer based on the DustCOMM-2021 dataset.**

It should be noted that the DustCOMM-2021 is a climatological dataset. As such the uncertainties included in this
940 dataset cannot be propagated into not propagable for instantaneous observational retrievals. Hence, in this study, instead of scaling the Di-Biagio RI's fractional contribution to form a new dust RI, we select the source region if its DAOD fractional contribution exceeds 0.1 and assign the corresponding Di-Biagio RIs within the selected source region for our retrieval. Figure C1 shows the nine regimes over oceans with fractional contribution greater than 0.1 for the nine defined dust source regions in summer (see Figures S2 to S4 for other seasons). The Di-Biagio RIs are
945 assigned to the nine source regions based on their geolocations. For observations in each season within each regime, the retrieval will assume the dust originated from the identified dust source regions and choose the corresponding Di-Biagio RIs. Note that the nine regimes can overlap, meaning that the observation over a particular grid cell covered by multiple regimes will assume multiple RIs from these regimes. The uncertainty due to the variation of multiple RIs is evaluated in Section 3.2.

950 **Data availability**

The 2007 to 2017 MODIS-CALIOP $DAOD_{10\mu m}$ and coarse-mode D_{eff} data (L2 and $5° \times 2°$ monthly L3) will be publicly available after the acceptance of this manuscript.

Author contribution

Conceptualization, J.Z. and Z.Z.; methodology, J.Z., Z.Z. and Y.H.; software, J.Z., Z.Z., Q.S. and C.W.; validation,
955 J.Z. and Z.Z.; formal analysis, J.Z.; investigation, J.Z., and Z.Z.; data curation, J.Z., Z.Z., J.F.K., C.D.B., C.R.; writing—original draft preparation, J.Z.; writing—review and editing, J.Z., Z.Z., Y.H., A.G., Q.S., C.W., J.F.K., C.D.B., C.R. and Y.D.; visualization, J.Z.; supervision, Z.Z., Y.H. and A.G.; project administration, Z.Z.; funding acquisition, Z.Z. All authors have read and agreed to the published version of the manuscript.

Declaration of Competing Interest

960 Zhibo Zhang reports that financial support was provided by NASA.

Acknowledgment

990   **References**

Adebiyi, A. A. and Kok, J. F.: Climate models miss most of the coarse dust in the atmosphere, Sci Adv, 6, eaaz9507, 10.1126/sciadv.aaz9507, 2020a.

Adebiyi, A. A., Kok, J. F., Wang, Y., Ito, A., Ridley, D. A., Nabat, P., and Zhao, C.: Dust Constraints from joint Observational-Modelling-experiMental analysis (DustCOMM): comparison with measurements and model
995   simulations, Atmos. Chem. Phys., 20, 829-863, 10.5194/acp-20-829-2020, 2020b.

Adebiyi, A., Kok, J. F., Murray, B. J., Ryder, C. L., Stuut, J.-B. W., Kahn, R. A., Knippertz, P., Formenti, P., Mahowald, N. M., Pérez García-Pando, C., Klose, M., Ansmann, A., Samset, B. H., Ito, A., Balkanski, Y., Di Biagio, C., Romanias, M. N., Huang, Y., and Meng, J.: A review of coarse mineral dust in the Earth system, Aeolian Res, 60, 100849, https://doi.org/10.1016/j.aeolia.2022.100849, 2023.

1000   Alizadeh-Choobari, O., Sturman, A., and Zawar-Reza, P.: A global satellite view of the seasonal distribution of mineral dust and its correlation with atmospheric circulation, Dynamics of Atmospheres and Oceans, 68, 20-34, https://doi.org/10.1016/j.dynatmoce.2014.07.002, 2014.

Amiri-Farahani, A., Allen, R. J., Neubauer, D., and Lohmann, U.: Impact of Saharan dust on North Atlantic marine stratocumulus clouds: importance of the semidirect effect, Atmos Chem Phys, 17, 6305-6322, 2017.

1005   Bagnold, R. A.: Threshold Speed and Grain Size, in: The Physics of Blown Sand and Desert Dunes, Springer Netherlands, Dordrecht, 85-95, 10.1007/978-94-009-5682-7_7, 1974.

Capelle, V., Chédin, A., Pondrom, M., Crevoisier, C., Armante, R., Crepeau, L., and Scott, N. A.: Infrared dust aerosol optical depth retrieved daily from IASI and comparison with AERONET over the period 2007–2016, Remote Sens Environ, 206, 15-32, https://doi.org/10.1016/j.rse.2017.12.008, 2018.

1010   Capelle, V., Chédin, A., Siméon, M., Tsamalis, C., Pierangelo, C., Pondrom, M., Crevoisier, C., Crepeau, L., and Scott, N. A.: Evaluation of IASI-derived dust aerosol characteristics over the tropical belt, Atmospheric Chemistry & Physics, 14, 2014.

Carlson, T. N.: The Saharan elevated mixed layer and its aerosol optical depth, The Open Atmospheric Science Journal, 10, 2016.

1015   Chédin, A., Capelle, V., Scott, N. A., and Todd, M. C.: Contribution of IASI to the Observation of Dust Aerosol Emissions (Morning and Nighttime) Over the Sahara Desert, J Geophys Res Atmospheres, 125, e2019JD032014, https://doi.org/10.1029/2019JD032014, 2020.

Chen, Y., Han, Y., and Weng, F.: Comparison of two transmittance algorithms in the community radiative transfer model: Application to AVHRR, J Geophys Res Atmospheres, 117, 10.1029/2011jd016656, 2012.

1020   Choobari, O. A., Zawar-Reza, P., and Sturman, A.: The global distribution of mineral dust and its impacts on the climate system: A review, Atmos Res, 138, 152-165, 10.1016/j.atmosres.2013.11.007, 2014.

Clarisse, L., Clerbaux, C., Franco, B., Hadji-Lazaro, J., Whitburn, S., Kopp, A. K., Hurtmans, D., and Coheur, P.-F.: A Decadal Data Set of Global Atmospheric Dust Retrieved From IASI Satellite Measurements, J Geophys Res Atmospheres, 124, 1618-1647, https://doi.org/10.1029/2018JD029701, 2019.

1025   Denjean, C., Cassola, F., Mazzino, A., Triquet, S., Chevaillier, S., Grand, N., Bourrianne, T., Momboisse, G., Sellegri, K., Schwarzenbock, A., Freney, E., Mallet, M., and Formenti, P.: Size distribution and optical properties of mineral dust aerosols transported in the western Mediterranean, Atmos. Chem. Phys., 16, 1081-1104, 10.5194/acp-16-1081-2016, 2016.

DeSouza-Machado, S. G., Strow, L. L., Hannon, S. E., and Motteler, H. E.: Infrared dust spectral signatures from
1030   AIRS, Geophys Res Lett, 33, 10.1029/2005gl024364, 2006.

Di Biagio, C., Banks, J. R., and Gaetani, M.: Dust Atmospheric Transport Over Long Distances, in: Reference Module in Earth Systems and Environmental Sciences, Elsevier, https://doi.org/10.1016/B978-0-12-818234-5.00033-X, 2021.

Di Biagio, C., Formenti, P., Balkanski, Y., Caponi, L., Cazaunau, M., Pangui, E., Journet, E., Nowak, S., Caquineau,
1035   S., Andreae, M. O., Kandler, K., Saeed, T., Piketh, S., Seibert, D., Williams, E., and Doussin, J.-F.: Global scale variability of the mineral dust long-wave refractive index: a new dataset of in situ measurements for climate modeling and remote sensing, Atmos Chem Phys, 17, 1901-1929, 10.5194/acp-17-1901-2017, 2017.

Ding, S., Yang, P., Weng, F., Liu, Q., Han, Y., van Delst, P., Li, J., and Baum, B.: Validation of the community radiative transfer model, J Quantitative Spectrosc Radiat Transf, 112, 1050-1064,
1040   https://doi.org/10.1016/j.jqsrt.2010.11.009, 2011.

Dubovik, O., Holben, B., Lapyonok, T., Sinyuk, A., Mishchenko, M., Yang, P., and Slutsker, I.: Non-spherical aerosol retrieval method employing light scattering by spheroids, Geophys Res Lett, 29, 54-51-54-54, 2002.

Dubovik, O., Sinyuk, A., Lapyonok, T., Holben, B. N., Mishchenko, M., Yang, P., Eck, T. F., Volten, H., Munoz, O.,
and Veihelmann, B.: Application of spheroid models to account for aerosol particle nonsphericity in remote
1045   sensing of desert dust, J Geophys Res Atmospheres, 111, 2006.
Garnier, A., Pelon, J., Dubuisson, P., Yang, P., Faivre, M., Chomette, O., Pascal, N., Lucker, P., and Murray, T.:
Retrieval of cloud properties using CALIPSO Imaging Infrared Radiometer: Part II: effective diameter and ice
water path, J. Appl. Meteor. Climatol., 52, 2582–2599, https://doi.org/10.1175/JAMC-D-12- 0328.1, 2013.
Gasteiger, J., Groß, S., Sauer, D., Haarig, M., Ansmann, A., and Weinzierl, B.: Particle settling and vertical mixing in
1050   the Saharan Air Layer as seen from an integrated model, lidar, and in situ perspective, Atmos. Chem. Phys.,
17, 297-311, 10.5194/acp-17-297-2017, 2017.
Gelaro, R., McCarty, W., Suárez, M. J., Todling, R., Molod, A., Takacs, L., Randles, C. A., Darmenov, A., Bosilovich,
M. G., Reichle, R., Wargan, K., Coy, L., Cullather, R., Draper, C., Akella, S., Buchard, V., Conaty, A., da
Silva, A. M., Gu, W., Kim, G.-K., Koster, R., Lucchesi, R., Merkova, D., Nielsen, J. E., Partyka, G., Pawson,
1055   S., Putman, W., Rienecker, M., Schubert, S. D., Sienkiewicz, M., and Zhao, B.: The Modern-Era Retrospective
Analysis for Research and Applications, Version 2 (MERRA-2), J Climate, 30, 5419-5454, 10.1175/jcli-d-16-
0758.1, 2017.
Ginoux, P.: Effects of nonsphericity on mineral dust modeling, J Geophys Res Atmospheres, 108,
https://doi.org/10.1029/2002JD002516, 2003.
1060   Ginoux, P., Garbuzov, D., and Hsu, N. C.: Identification of anthropogenic and natural dust sources using Moderate
Resolution Imaging Spectroradiometer (MODIS) Deep Blue level 2 data, Journal of Geophysical Research-
Atmospheres, 115, 10.1029/2009jd012398, 2010.
Ginoux, P., Prospero, J. M., Gill, T. E., Hsu, N. C., and Zhao, M.: Global-scale attribution of anthropogenic and natural
dust sources and their emission rates based on MODIS Deep Blue aerosol products, Reviews of Geophysics,
1065   50, https://doi.org/10.1029/2012RG000388, 2012.
Gkikas, A., Proestakis, E., Amiridis, V., Kazadzis, S., Di Tomaso, E., Tsekeri, A., Marinou, E., Hatzianastassiou, N.,
and Pérez García-Pando, C.: ModIs Dust AeroSol (MIDAS): a global fine-resolution dust optical depth data
set, Atmos. Meas. Tech., 14, 309-334, 10.5194/amt-14-309-2021, 2021.
Gkikas, A., Proestakis, E., Amiridis, V., Kazadzis, S., Di Tomaso, E., Marinou, E., Hatzianastassiou, N., Kok, J. F.,
1070   and Garcia-Pando, C. P.: Quantification of the dust optical depth across spatiotemporal scales with the MIDAS
global dataset (2003-2017), Atmos Chem Phys, 22, 3553-3578, 10.5194/acp-22-3553-2022, 2022.
Goudie, A.: Dust storms in space and time, Progress in Physical Geography, 7, 502-530, 1983.
Grogan, D. F. P., Nathan, T. R., and Chen, S.-H.: Effects of Saharan Dust on the Linear Dynamics of African Easterly
Waves, J Atmos Sci, 73, 891-911, 10.1175/jas-d-15-0143.1, 2016.
1075   Gutleben, M. and Groß, S.: Turbulence Analysis in Long-Range-Transported Saharan Dust Layers With Airborne
Lidar, Geophys Res Lett, 48, e2021GL094418, https://doi.org/10.1029/2021GL094418, 2021.
Haarig, M., Ansmann, A., Engelmann, R., Baars, H., Toledano, C., Torres, B., Althausen, D., Radenz, M., and
Wandinger, U.: First triple-wavelength lidar observations of depolarization and extinction-to-backscatter ratios
of Saharan dust, Atmos. Chem. Phys., 22, 355-369, 10.5194/acp-22-355-2022, 2022.
1080   Haarig, M., Ansmann, A., Gasteiger, J., Kandler, K., Althausen, D., Baars, H., Radenz, M., and Farrell, D. A.: Dry
versus wet marine particle optical properties: RH dependence of depolarization ratio, backscatter, and
extinction from multiwavelength lidar measurements during SALTRACE, Atmos. Chem. Phys., 17, 14199-
14217, 10.5194/acp-17-14199-2017, 2017.
Han, Y.: JCSDA community radiative transfer model (CRTM): Version 1, 2006.
1085   Hansen, J., Sato, M., and Ruedy, R.: Radiative forcing and climate response, J Geophys Res Atmospheres, 102, 6831-
6864, 1997.
Hansen, J. E. and Travis, L. D.: Light scattering in planetary atmospheres, Space Science Reviews, 16, 527-610,
10.1007/BF00168069, 1974.
Hao, M. and Mendel, J. M.: Linguistic Weighted Standard Deviation, 2013 Joint IFSA World Congress and NAFIPS
1090   Annual Meeting (IFSA/NAFIPS), 24-28 June 2013, 108-113, 10.1109/IFSA-NAFIPS.2013.6608384,
Heckert, N. and Filliben, J.: Dataplot Reference Manual, Volume 2: Let Subcommands and Library Functions,
Technical Report 148, National Institute of Standards and Technology, 2003.
Helmert, J., Heinold, B., Tegen, I., Hellmuth, O., and Wendisch, M.: On the direct and semidirect effects of Saharan
dust   over   Europe: A   modeling   study,   J   Geophys   Res   Atmospheres,   112,
1095   https://doi.org/10.1029/2006JD007444, 2007.
Hsu, N. C., Jeong, M.-J., Bettenhausen, C., Sayer, A. M., Hansell, R., Seftor, C. S., Huang, J., and Tsay, S.-C.:
Enhanced Deep Blue aerosol retrieval algorithm: The second generation, J Geophys Res Atmospheres, 118,
9296-9315, https://doi.org/10.1002/jgrd.50712, 2013.

1100 Huang, H., Qian, Y., Liu, Y., He, C., Zheng, J., Zhang, Z., and Gkikas, A.: Where does the dust deposited over the Sierra Nevada snow come from?, EGUsphere, 2022, 1-38, 10.5194/egusphere-2022-588, 2022.

Huang, Y., Kok, J. F., Kandler, K., Lindqvist, H., Nousiainen, T., Sakai, T., Adebiyi, A., and Jokinen, O.: Climate Models and Remote Sensing Retrievals Neglect Substantial Desert Dust Asphericity, Geophys Res Lett, 47, e2019GL086592, https://doi.org/10.1029/2019GL086592, 2020.

1105 Huneeus, N., Schulz, M., Balkanski, Y., Griesfeller, J., Prospero, J., Kinne, S., Bauer, S., Boucher, O., Chin, M., Dentener, F., Diehl, T., Easter, R., Fillmore, D., Ghan, S., Ginoux, P., Grini, A., Horowitz, L., Koch, D., Krol, M. C., Landing, W., Liu, X., Mahowald, N., Miller, R., Morcrette, J. J., Myhre, G., Penner, J., Perlwitz, J., Stier, P., Takemura, T., and Zender, C. S.: Global dust model intercomparison in AeroCom phase I, Atmos. Chem. Phys., 11, 7781-7816, 10.5194/acp-11-7781-2011, 2011.

Journet, E., Balkanski, Y., and Harrison, S. P.: A new data set of soil mineralogy for dust-cycle modeling, Atmos.
1110 Chem. Phys., 14, 3801-3816, 10.5194/acp-14-3801-2014, 2014.

Kahn, R. A., Gaitley, B. J., Garay, M. J., Diner, D. J., Eck, T. F., Smirnov, A., and Holben, B. N.: Multiangle Imaging SpectroRadiometer global aerosol product assessment by comparison with the Aerosol Robotic Network, J Geophys Res Atmospheres, 115, https://doi.org/10.1029/2010JD014601, 2010.

Kaufman, Y. J., Koren, I., Remer, L. A., Tanre, D., Ginoux, P., and Fan, S.: Dust transport and deposition observed
1115 from the Terra-Moderate Resolution Imaging Spectroradiometer (MODIS) spacecraft over the Atlantic ocean, Journal of Geophysical Research-Atmospheres, 110, 10.1029/2003jd004436, 2005.

Kim, M.-H., Kim, S.-W., and Omar, A. H.: Dust Lidar Ratios Retrieved from the CALIOP Measurements Using the MODIS AOD as a Constraint, Remote Sens-basel, 12, 251, 2020.

Kim, M.-H., Omar, A. H., Tackett, J. L., Vaughan, M. A., Winker, D. M., Trepte, C. R., Hu, Y., Liu, Z., Poole, L. R.,
1120 and Pitts, M. C.: The CALIPSO version 4 automated aerosol classification and lidar ratio selection algorithm, Atmos Meas Tech, 11, 6107, 2018.

Kinne, S., Schulz, M., Textor, C., Guibert, S., Balkanski, Y., Bauer, S. E., Berntsen, T., Berglen, T. F., Boucher, O., Chin, M., Collins, W., Dentener, F., Diehl, T., Easter, R., Feichter, J., Fillmore, D., Ghan, S., Ginoux, P., Gong, S., Grini, A., Hendricks, J., Herzog, M., Horowitz, L., Isaksen, I., Iversen, T., Kirkevåg, A., Kloster, S., Koch,
1125 D., Kristjansson, J. E., Krol, M., Lauer, A., Lamarque, J. F., Lesins, G., Liu, X., Lohmann, U., Montanaro, V., Myhre, G., Penner, J., Pitari, G., Reddy, S., Seland, O., Stier, P., Takemura, T., and Tie, X.: An AeroCom initial assessment – optical properties in aerosol component modules of global models, Atmos. Chem. Phys., 6, 1815-1834, 10.5194/acp-6-1815-2006, 2006.

Kok, J. F., Adebiyi, A. A., Albani, S., Balkanski, Y., Checa-Garcia, R., Chin, M., Colarco, P. R., Hamilton, D. S.,
1130 Huang, Y., Ito, A., Klose, M., Li, L., Mahowald, N. M., Miller, R. L., Obiso, V., Pérez García-Pando, C., Rocha-Lima, A., and Wan, J. S.: Contribution of the world's main dust source regions to the global cycle of desert dust, Atmos. Chem. Phys., 21, 8169-8193, 10.5194/acp-21-8169-2021, 2021a.

Kok, J. F., Adebiyi, A. A., Albani, S., Balkanski, Y., Checa-Garcia, R., Chin, M., Colarco, P. R., Hamilton, D. S., Huang, Y., Ito, A., Klose, M., Leung, D. M., Li, L., Mahowald, N. M., Miller, R. L., Obiso, V., Pérez García-
1135 Pando, C., Rocha-Lima, A., Wan, J. S., and Whicker, C. A.: Improved representation of the global dust cycle using observational constraints on dust properties and abundance, Atmos. Chem. Phys., 21, 8127-8167, 10.5194/acp-21-8127-2021, 2021b.

Levy, R., Mattoo, S., Munchak, L., Remer, L., Sayer, A., Patadia, F., and Hsu, N.: The Collection 6 MODIS aerosol products over land and ocean, Atmos Meas Tech, 6, 2989-3034, 2013.

1140 Li, L., Mahowald, N. M., Miller, R. L., Pérez García-Pando, C., Klose, M., Hamilton, D. S., Gonçalves Ageitos, M., Ginoux, P., Balkanski, Y., Green, R. O., Kalashnikova, O., Kok, J. F., Obiso, V., Paynter, D., and Thompson, D. R.: Quantifying the range of the dust direct radiative effect due to source mineralogy uncertainty, Atmos. Chem. Phys., 21, 3973-4005, 10.5194/acp-21-3973-2021, 2021.

Liang, X., Ignatov, A., Kramar, M., and Yu, F.: Preliminary Inter-Comparison between AHI, VIIRS and MODIS
1145 Clear-Sky Ocean Radiances for Accurate SST Retrievals, Remote Sens-basel, 8, 203, 2016.

Liu, C., Panetta, R. L., Yang, P., Macke, A., and Baran, A. J.: Modeling the scattering properties of mineral aerosols using concave fractal polyhedra, Appl Optics, 52, 640-652, 2013.

Liu, Z., Sugimoto, N., and Murayama, T.: Extinction-to-backscatter ratio of Asian dust observed with high-spectral-resolution lidar and Raman lidar, Appl Optics, 41, 2760-2767, 2002.

1150 Liu, Z., Kar, J., Zeng, S., Tackett, J., Vaughan, M., Avery, M., Pelon, J., Getzewich, B., Lee, K.-P., and Magill, B.: Discriminating between clouds and aerosols in the CALIOP version 4.1 data products, 2019.

Liu, Z., Omar, A., Vaughan, M., Hair, J., Kittaka, C., Hu, Y., Powell, K., Trepte, C., Winker, D., Hostetler, C., Ferrare, R., and Pierce, R.: CALIPSO lidar observations of the optical properties of Saharan dust: A case study of long-range transport, J Geophys Res Atmospheres, 113, https://doi.org/10.1029/2007JD008878, 2008.

1155   Logothetis, S. A., Salamalikis, V., Gkikas, A., Kazadzis, S., Amiridis, V., and Kazantzidis, A.: 15-year variability of
            desert dust optical depth on global and regional scales, Atmos Chem Phys, 21, 16499-16529, 10.5194/acp-21-
            16499-2021, 2021.
        Luo, B., Minnett, P. J., Gentemann, C., and Szczodrak, G.: Improving satellite retrieved night-time infrared sea surface
            temperatures   in   aerosol   contaminated   regions,   Remote   Sens   Environ,   223,   8-20,
1160   https://doi.org/10.1016/j.rse.2019.01.009, 2019.
        Madhavan, S., Xiong, X., Wu, A., Wenny, B. N., Chiang, K., Chen, N., Wang, Z., and Li, Y.: Noise Characterization
            and Performance of MODIS Thermal Emissive Bands, Ieee T Geosci Remote, 54, 3221-3234,
            10.1109/TGRS.2015.2514061, 2016.
        Mahowald, N., Albani, S., Kok, J. F., Engelstaeder, S., Scanza, R., Ward, D. S., and Flanner, M. G.: The size
1165   distribution of desert dust aerosols and its impact on the Earth system, Aeolian Res, 15, 53-71,
            10.1016/j.aeolia.2013.09.002, 2014.
        Marticorena, B., Chatenet, B., Rajot, J. L., Traoré, S., Coulibaly, M., Diallo, A., Koné, I., Maman, A., Ndiaye, T., and
            Zakou, A.: Temporal variability of mineral dust concentrations over West Africa: analyses of a pluriannual
            monitoring from the AMMA Sahelian Dust Transect, Atmos. Chem. Phys., 10, 8899-8915, 10.5194/acp-10-
1170   8899-2010, 2010.
        McConnell, C. L., Highwood, E. J., Coe, H., Formenti, P., Anderson, B., Osborne, S., Nava, S., Desboeufs, K., Chen,
            G., and Harrison, M. A. J.: Seasonal variations of the physical and optical characteristics of Saharan dust:
            Results from the Dust Outflow and Deposition to the Ocean (DODO) experiment, J Geophys Res Atmospheres,
            113, https://doi.org/10.1029/2007JD009606, 2008.
1175   McMillin, L. M., Xiong, X., Han, Y., Kleespies, T. J., and Van Delst, P.: Atmospheric transmittance of an absorbing
            gas. 7. Further improvements to the OPTRAN 6 approach, Appl Optics, 45, 2028-2034,
            10.1364/AO.45.002028, 2006.
        Meng, Z., Yang, P., Kattawar, G. W., Bi, L., Liou, K., and Laszlo, I.: Single-scattering properties of tri-axial ellipsoidal
            mineral dust aerosols: A database for application to radiative transfer calculations, Journal of Aerosol Science,
1180   41, 501-512, 2010.
        Miller, R. L. and Tegen, I.: Climate Response to Soil Dust Aerosols, J Climate, 11, 3247-3267, 10.1175/1520-
            0442(1998)011<3247:Crtsda>2.0.Co;2, 1998.
        Mishchenko, M. I., Travis, L. D., and Mackowski, D. W.: T-matrix computations of light scattering by nonspherical
            particles: A review, J Quantitative Spectrosc Radiat Transf, 55, 535-575, https://doi.org/10.1016/0022-
1185   4073(96)00002-7, 1996.
        Mishchenko, M. I., Travis, L. D., Kahn, R. A., and West, R. A.: Modeling phase functions for dustlike tropospheric
            aerosols using a shape mixture of randomly oriented polydisperse spheroids, J Geophys Res Atmospheres, 102,
            16831-16847, 1997.
        Müller, D., Lee, K.-H., Gasteiger, J., Tesche, M., Weinzierl, B., Kandler, K., Müller, T., Toledano, C., Otto, S.,
1190   Althausen, D., and Ansmann, A.: Comparison of optical and microphysical properties of pure Saharan mineral
            dust observed with AERONET Sun photometer, Raman lidar, and in situ instruments during SAMUM 2006, J
            Geophys Res Atmospheres, 117, https://doi.org/10.1029/2011JD016825, 2012.
        Müller, D., Weinzierl, B., Petzold, A., Kandler, K., Ansmann, A., Müller, T., Tesche, M., Freudenthaler, V., Esselborn,
            M., Heese, B., Althausen, D., Schladitz, A., Otto, S., and Knippertz, P.: Mineral dust observed with AERONET
1195   Sun photometer, Raman lidar, and in situ instruments during SAMUM 2006: Shape-independent particle
            properties, J Geophys Res Atmospheres, 115, https://doi.org/10.1029/2009JD012520, 2010.
        Nousiainen, T. and Kandler, K.: Light scattering by atmospheric mineral dust particles, in: Light Scattering Reviews
            9: Light Scattering and Radiative Transfer, edited by: Kokhanovsky, A. A., Springer Berlin Heidelberg, Berlin,
            Heidelberg, 3-52, 10.1007/978-3-642-37985-7_1, 2015.
1200   O'Carroll, A. G., Armstrong, E. M., Beggs, H. M., Bouali, M., Casey, K. S., Corlett, G. K., Dash, P., Donlon, C. J.,
            Gentemann, C. L., Høyer, J. L., Ignatov, A., Kabobah, K., Kachi, M., Kurihara, Y., Karagali, I., Maturi, E.,
            Merchant, C. J., Marullo, S., Minnett, P. J., Pennybacker, M., Ramakrishnan, B., Ramsankaran, R., Santoleri,
            R., Sunder, S., Picart, S. S., Vázquez-Cuervo, J., and Wimmer, W.: Observational Needs of Sea Surface
            Temperature, Frontiers Mar Sci, 6, 420, 10.3389/fmars.2019.00420, 2019.
1205   Paepe, B. D. and Dewitte, S.: Dust Aerosol Optical Depth Retrieval over a Desert Surface Using the SEVIRI Window
            Channels, J Atmos Ocean Tech, 26, 704-718, 10.1175/2008jtecha1109.1, 2009.
        Pavolonis, M. J., Heidinger, A. K., and Sieglaff, J.: Automated retrievals of volcanic ash and dust cloud properties
            from upwelling infrared measurements, J Geophys Res Atmospheres, 118, 1436-1458,
            https://doi.org/10.1002/jgrd.50173, 2013.

1210   Pavolonis, M. J., Sieglaff, J., and Cintineo, J.: Spectrally Enhanced Cloud Objects—A generalized framework for automated detection of volcanic ash and dust clouds using passive satellite measurements: 1. Multispectral analysis, J Geophys Res Atmospheres, 120, 7813-7841, https://doi.org/10.1002/2014JD022968, 2015.

Peyridieu, S., Chédin, A., Tanré, D., Capelle, V., Pierangelo, C., Lamquin, N., and Armante, R.: Saharan dust infrared optical depth and altitude retrieved from AIRS: a focus over North Atlantic – comparison to MODIS
1215   and CALIPSO, Atmos Chem Phys, 10, 1953-1967, 10.5194/acp-10-1953-2010, 2010.

Peyridieu, S., Chédin, A., Capelle, V., Tsamalis, C., Pierangelo, C., Armante, R., Crevoisier, C., Crépeau, L., Siméon, M., Ducos, F., and Scott, N. A.: Characterisation of dust aerosols in the infrared from IASI and comparison with PARASOL, MODIS, MISR, CALIOP, and AERONET observations, Atmos. Chem. Phys., 13, 6065-6082, 10.5194/acp-13-6065-2013, 2013.

1220   Pierangelo, C., Mishchenko, M., Balkanski, Y., and Chédin, A.: Retrieving the effective radius of Saharan dust coarse mode from AIRS, Geophys Res Lett, 32, 10.1029/2005gl023425, 2005.

Pierangelo, C., Chédin, A., Heilliette, S., Jacquinet-Husson, N., and Armante, R.: Dust altitude and infrared optical depth from AIRS, Atmos Chem Phys, 4, 1813-1822, 10.5194/acp-4-1813-2004, 2004.

Proestakis, E., Amiridis, V., Marinou, E., Georgoulias, A. K., Solomos, S., Kazadzis, S., Chimot, J., Che, H. Z.,
1225   Alexandri, G., Binietoglou, I., Daskalopoulou, V., Kourtidis, K. A., de Leeuw, G., and Ronald, J. V.: Nine-year spatial and temporal evolution of desert dust aerosols over South and East Asia as revealed by CALIOP, Atmos Chem Phys, 18, 1337-1362, 10.5194/acp-18-1337-2018, 2018.

Pu, B. and Ginoux, P.: How reliable are CMIP5 models in simulating dust optical depth?, Atmos. Chem. Phys., 18, 12491-12510, 10.5194/acp-18-12491-2018, 2018.

1230   Ridley, D. A., Heald, C. L., Kok, J. F., and Zhao, C.: An observationally constrained estimate of global dust aerosol optical depth, Atmos. Chem. Phys., 16, 15097-15117, 10.5194/acp-16-15097-2016, 2016.

Ryder, C. L., Highwood, E. J., Lai, T. M., Sodemann, H., and Marsham, J. H.: Impact of atmospheric transport on the evolution of microphysical and optical properties of Saharan dust, Geophys Res Lett, 40, 2433-2438, https://doi.org/10.1002/grl.50482, 2013a.

1235   Ryder, C. L., Highwood, E. J., Walser, A., Seibert, P., Philipp, A., and Weinzierl, B.: Coarse and giant particles are ubiquitous in Saharan dust export regions and are radiatively significant over the Sahara, Atmos. Chem. Phys., 19, 15353-15376, 10.5194/acp-19-15353-2019, 2019.

Ryder, C. L., Highwood, E. J., Rosenberg, P. D., Trembath, J., Brooke, J. K., Bart, M., Dean, A., Crosier, J., Dorsey, J., Brindley, H., Banks, J., Marsham, J. H., McQuaid, J. B., Sodemann, H., and Washington, R.: Optical
1240   properties of Saharan dust aerosol and contribution from the coarse mode as measured during the Fennec 2011 aircraft campaign, Atmos Chem Phys, 13, 303-325, 10.5194/acp-13-303-2013, 2013b.

Ryder, C. L., Marenco, F., Brooke, J. K., Estelles, V., Cotton, R., Formenti, P., McQuaid, J. B., Price, H. C., Liu, D., Ausset, P., Rosenberg, P. D., Taylor, J. W., Choularton, T., Bower, K., Coe, H., Gallagher, M., Crosier, J., Lloyd, G., Highwood, E. J., and Murray, B. J.: Coarse-mode mineral dust size distributions, composition and
1245   optical properties from AER-D aircraft measurements over the tropical eastern Atlantic, Atmos. Chem. Phys., 18, 17225-17257, 10.5194/acp-18-17225-2018, 2018.

Saito, M., Yang, P., Ding, J., and Liu, X.: A Comprehensive Database of the Optical Properties of Irregular Aerosol Particles for Radiative Transfer Simulations, J Atmos Sci, 78, 2089-2111, 10.1175/jas-d-20-0338.1, 2021.

Scheuvens, D. and Kandler, K.: On composition, morphology, and size distribution of airborne mineral dust, Mineral
1250   Dust, 15-49, 2014.

Scott, N. A. and Chedin, A.: A Fast Line-by-Line Method for Atmospheric Absorption Computations: The Automatized Atmospheric Absorption Atlas, J Appl Meteorol, 20, 802-812, 10.1175/1520-0450(1981)020<0802:aflblm>2.0.co;2, 1981.

Shao, Y., Wyrwoll, K.-H., Chappell, A., Huang, J., Lin, Z., McTainsh, G. H., Mikami, M., Tanaka, T. Y., Wang, X.,
1255   and Yoon, S.: Dust cycle: An emerging core theme in Earth system science, Aeolian Res, 2, 181-204, 2011.

Sokolik, I. N. and Toon, O. B.: Incorporation of mineralogical composition into models of the radiative properties of mineral aerosol from UV to IR wavelengths, J Geophys Res Atmospheres, 104, 9423-9444, 1999.

Song, Q., Zhang, Z., Yu, H., Kato, S., Yang, P., Colarco, P., Remer, L. A., and Ryder, C. L.: Net radiative effects of dust in the tropical North Atlantic based on integrated satellite observations and in situ measurements, Atmos
1260   Chem Phys, 18, 11303-11322, 10.5194/acp-18-11303-2018, 2018.

Song, Q., Zhang, Z., Yu, H., Kok, J. F., Di Biagio, C., Albani, S., Zheng, J., and Ding, J.: Size-resolved dust direct radiative effect efficiency derived from satellite observations, Atmos. Chem. Phys., 22, 13115-13135, 10.5194/acp-22-13115-2022, 2022.

Song, Q. Q., Zhang, Z. B., Yu, H. B., Ginoux, P., and Shen, J.: Global dust optical depth climatology derived from CALIOP and MODIS aerosol retrievals on decadal timescales: regional and interannual variability, Atmos Chem Phys, 21, 13369-13395, 10.5194/acp-21-13369-2021, 2021.

Stamnes, K., Tsay, S. C., Wiscombe, W., and Jayaweera, K.: Numerically stable algorithm for discrete-ordinate-method radiative transfer in multiple scattering and emitting layered media, Appl Optics, 27, 2502-2509, 10.1364/ao.27.002502 PMID - 20531783, 1988.

Stein, A., Draxler, R. R., Rolph, G. D., Stunder, B. J., Cohen, M., and Ngan, F.: NOAA's HYSPLIT atmospheric transport and dispersion modeling system, B Am Meteorol Soc, 96, 2059-2077, 2015.

Tegen, I. and Fung, I.: Modeling of mineral dust in the atmosphere: Sources, transport, and optical thickness, J Geophys Res Atmospheres, 99, 22897-22914, 10.1029/94jd01928, 1994.

Toledano, C., Torres, B., Velasco-Merino, C., Althausen, D., Groß, S., Wiegner, M., Weinzierl, B., Gasteiger, J., Ansmann, A., González, R., Mateos, D., Farrel, D., Müller, T., Haarig, M., and Cachorro, V. E.: Sun photometer retrievals of Saharan dust properties over Barbados during SALTRACE, Atmos. Chem. Phys., 19, 14571-14583, 10.5194/acp-19-14571-2019, 2019.

Uno, I., Eguchi, K., Yumimoto, K., Takemura, T., Shimizu, A., Uematsu, M., Liu, Z., Wang, Z., Hara, Y., and Sugimoto, N.: Asian dust transported one full circuit around the globe, Nature Geoscience, 2, 557-560, 10.1038/ngeo583, 2009.

van der Does, M., Knippertz, P., Zschenderlein, P., Giles Harrison, R., and Stuut, J.-B. W.: The mysterious long-range transport of giant mineral dust particles, Sci Adv, 4, eaau2768, doi:10.1126/sciadv.aau2768, 2018.

Wang, C., Platnick, S., Zhang, Z., Meyer, K., and Yang, P.: Retrieval of ice cloud properties using an optimal estimation algorithm and MODIS infrared observations: 1. Forward model, error analysis, and information content, J Geophys Res Atmospheres, 121, 5809-5826, 2016.

Weinzierl, B., Ansmann, A., Prospero, J. M., Althausen, D., Benker, N., Chouza, F., Dollner, M., Farrell, D., Fomba, W. K., Freudenthaler, V., Gasteiger, J., Groß, S., Haarig, M., Heinold, B., Kandler, K., Kristensen, T. B., Mayol-Bracero, O. L., Müller, T., Reitebuch, O., Sauer, D., Schäfler, A., Schepanski, K., Spanu, A., Tegen, I., Toledano, C., and Walser, A.: The Saharan Aerosol Long-Range Transport and Aerosol–Cloud-Interaction Experiment: Overview and Selected Highlights, B Am Meteorol Soc, 98, 1427-1451, 10.1175/bams-d-15-00142.1, 2017.

Wentz, F. and Meissner, T.: AMSR ocean algorithm theoretical basis document, version 2, report, Remote Sens, Syst., Santa Rosa, Calif, 2000.

Winker, D. M., Tackett, J. L., Getzewich, B. J., Liu, Z., Vaughan, M. A., and Rogers, R. R.: The global 3-D distribution of tropospheric aerosols as characterized by CALIOP, Atmos. Chem. Phys., 13, 3345-3361, 10.5194/acp-13-3345-2013, 2013.

Winker, D. M., Vaughan, M. A., Omar, A., Hu, Y., Powell, K. A., Liu, Z., Hunt, W. H., and Young, S. A.: Overview of the CALIPSO Mission and CALIOP Data Processing Algorithms, J Atmos Ocean Tech, 26, 2310-2323, 10.1175/2009jtecha1281.1, 2009.

Woodage, M. J. and Woodward, S.: U.K. HiGEM: Impacts of Desert Dust Radiative Forcing in a High-Resolution Atmospheric GCM, J Climate, 27, 5907-5928, 10.1175/jcli-d-13-00556.1, 2014.

Woodward, S.: Modeling the atmospheric life cycle and radiative impact of mineral dust in the Hadley Centre climate model, J Geophys Res Atmospheres, 106, 18155-18166, https://doi.org/10.1029/2000JD900795, 2001.

Xia, W., Wang, Y., and Wang, B.: Decreasing Dust Over the Middle East Partly Caused by Irrigation Expansion, Earth's Future, 10, e2021EF002252, https://doi.org/10.1029/2021EF002252, 2022.

Xiong, X., Wenny, B. N., Wu, A., Barnes, W. L., and Salomonson, V. V.: Aqua MODIS Thermal Emissive Band On-Orbit Calibration, Characterization, and Performance, Ieee T Geosci Remote, 47, 803-814, 10.1109/TGRS.2008.2005109, 2009.

Yang, Z., Wang, J., Ichoku, C., Hyer, E., and Zeng, J.: Mesoscale modeling and satellite observation of transport and mixing of smoke and dust particles over northern sub-Saharan African region, J Geophys Res Atmospheres, 118, 12,139-112,157, https://doi.org/10.1002/2013JD020644, 2013.

Yu, H., Remer, L. A., Kahn, R. A., Chin, M., and Zhang, Y.: Satellite perspective of aerosol intercontinental transport: From qualitative tracking to quantitative characterization, Atmos Res, 124, 73-100, https://doi.org/10.1016/j.atmosres.2012.12.013, 2013.

Yu, H., Chin, M., Remer, L. A., Kleidman, R. G., Bellouin, N., Bian, H., and Diehl, T.: Variability of marine aerosol fine-mode fraction and estimates of anthropogenic aerosol component over cloud-free oceans from the Moderate Resolution Imaging Spectroradiometer (MODIS), J Geophys Res Atmospheres, 114, https://doi.org/10.1029/2008JD010648, 2009.

Yu, H., Chin, M., Winker, D. M., Omar, A. H., Liu, Z., Kittaka, C., and Diehl, T.: Global view of aerosol vertical distributions from CALIPSO lidar measurements and GOCART simulations: Regional and seasonal variations, J Geophys Res Atmospheres, 115, https://doi.org/10.1029/2009JD013364, 2010.

Yu, H., Chin, M., Bian, H., Yuan, T., Prospero, J. M., Omar, A. H., Remer, L. A., Winker, D. M., Yang, Y., and Zhang, Y.: Quantification of trans-Atlantic dust transport from seven-year (2007–2013) record of CALIPSO lidar measurements, Remote Sens Environ, 159, 232-249, 2015a.

Yu, H., Chin, M., Bian, H., Yuan, T., Prospero, J. M., Omar, A. H., Remer, L. A., Winker, D. M., Yang, Y., Zhang, Y., and Zhang, Z.: Quantification of trans-Atlantic dust transport from seven-year (2007–2013) record of CALIPSO lidar measurements, Remote Sens Environ, 159, 232-249, 10.1016/j.rse.2014.12.010, 2015b.

Yu, H., Tan, Q., Chin, M., Remer, L. A., Kahn, R. A., Bian, H., Kim, D., Zhang, Z., Yuan, T., Omar, A. H., Winker, D. M., Levy, R. C., Kalashnikova, O., Crepeau, L., Capelle, V., and Chédin, A.: Estimates of African Dust Deposition Along the Trans-Atlantic Transit Using the Decadelong Record of Aerosol Measurements from CALIOP, MODIS, MISR, and IASI, J Geophys Res Atmospheres, 124, 7975-7996, https://doi.org/10.1029/2019JD030574, 2019.

Yu, Y., Kalashnikova, O. V., Garay, M. J., Lee, H., Choi, M., Okin, G. S., Yorks, J. E., Campbell, J. R., and Marquis, J.: A global analysis of diurnal variability in dust and dust mixture using CATS observations, Atmos. Chem. Phys., 21, 1427-1447, 10.5194/acp-21-1427-2021, 2021.

Zhang, H., McFarquhar, G. M., Saleeby, S. M., and Cotton, W. R.: Impacts of Saharan dust as CCN on the evolution of an idealized tropical cyclone, Geophys Res Lett, 34, 2007.

Zhang, P., Lu, N.-m., Hu, X.-q., and Dong, C.-h.: Identification and physical retrieval of dust storm using three MODIS thermal IR channels, Global Planet Change, 52, 197-206, 10.1016/j.gloplacha.2006.02.014, 2006.

Zheng, J., Huang, X., Sangondimath, S., Wang, J., and Zhang, Z.: Efficient and Flexible Aggregation and Distribution of MODIS Atmospheric Products Based on Climate Analytics as a Service Framework, Remote Sens-basel, 13, 3541, 2021.

Zheng, J., Zhang, Z., Garnier, A., Yu, H., Song, Q., Wang, C., Dubuisson, P., and Di Biagio, C.: The thermal infrared optical depth of mineral dust retrieved from integrated CALIOP and IIR observations, Remote Sens Environ, 270, 112841, https://doi.org/10.1016/j.rse.2021.112841, 2022.

Zhou, Y., Levy, R. C., Remer, L. A., Mattoo, S., Shi, Y., and Wang, C.: Dust Aerosol Retrieval Over the Oceans With the MODIS/VIIRS Dark-Target Algorithm: 1. Dust Detection, Earth and Space Science, 7, e2020EA001221, https://doi.org/10.1029/2020EA001221, 2020.

Zhou, Y., Levy, R. C., Remer, L. A., Mattoo, S., and Espinosa, W. R.: Dust Aerosol Retrieval Over the Oceans With the MODIS/VIIRS Dark Target Algorithm: 2. Nonspherical Dust Model, Earth and Space Science, 7, e2020EA001222, https://doi.org/10.1029/2020EA001222, 2020.